Russian Chemical Reviews **75** (10) 847 – 862 (2006) © 2006 Russian Academy of Sciences and Turpion Ltd

DOI 10.1070/RC2006v075n10ABEH003626

New materials for SRS lasers

T T Basiev, V V Osiko

Contents

I.	Introduction. Modern solid-state lasers	847
II.	The laser wavelength conversion using stimulated Raman light scattering	849
III.	The preparation and characterisation of single crystals of calcium, strontium, barium and lead molybdates and tungstates for SRS lasers	852
IV.	Raman scattering spectra of calcium, strontium, barium and lead molybdates and tungstates	854
V.	SRS converters and lasers based on novel crystals	860

Abstract. The problem of search for new materials for spectrally positioned laser sources, which is central for modern photonics, is discussed. The use of the stimulated Raman scattering effect in crystals offers a highly efficient way to the design of such sources. The recent results of investigations into this effect for a large number of various types of crystalline materials are presented. The most promising compounds, as regards the realisation of different laser operation modes, are considered, including calcium, strontium, barium and lead molybdates and tungstates. Several examples of functioning efficient lasers based on novel materials exhibiting the stimulated Raman light scattering effect are given. The bibliography includes 50 references.

I. Introduction. Modern solid-state lasers

Photonics is one of the most rapidly emerging fields within modern high technologies. Generally, the term photonics refers to techniques for the generation and conversion of light or other types of electromagnetic radiation. Over the recent years, photonics has experienced an explosive growth. Partly, this is due to the fact that it determines to a large extent the progress in such fields as medical, environmental and scientific instrument production, advanced technologies of materials processing and armament industry. But the most important reason is that photonics ever deeper penetrates into the information technologies, *i.e.*, the techniques used for the information acquisition, storage, processing, transmission and retrieval. Furthermore, many experts believe that it is photonics that will determine the cutting edge of informatics in the future. This forecast is based on the unprecedented high performance, information capacity and noise immunity provided by photonic devices. The greatest contribution to the emergence of photonics was made in the middle of the 20th century by academicians A M Prokhorov and N G Basov and by an American scientist, professor Ch Townes, who laid the foundations of quantum electronics and laser physics (these achievements were recognised with the Nobel prize in physics for 1964). These pioneering results gave rise to the development of various types of lasers exploiting substances in all possible aggregate states, *i.e.*, plasma, gas, vapour, crystal, glass and liquid, as working media. More recently, academician Zh I Alferov invented semiconducting heterostructures (the Nobel prize in physics for 2000 shared with H Kroemer and J S Kilby), which enabled the miniaturisation and functional integration of photonic devices.

It is dielectric and semiconducting crystals and structures derived from them that are the most typical materials used in photonics.[1] Crystals are superior to other types of materials due to the following factors:

— a high density of active particles (*e.g.*, atoms, ions, molecules, atomic clusters), which can be as high as 10^{23} cm^{-3}; this provides the small size of photonic devices and a possibility of their further miniaturisation and functional integration;

— a regular periodic packing of atoms (ions, molecules), which gives rise to symmetric structures and degenerate energy levels and, consequently, to narrow resonances and large photon absorption and emission cross-sections and also to large nonlinear optical coefficients;

— a variety of possible compositions (in particular, a huge number of combinations of crystalline matrices and active dopants) and crystal structures.

Contemporary photonics is an extended research field with numerous subfields. It is next to impossible to comprehensively address the multitude of directions of photonics development in one paper. Therefore, in the present review, we limit ourselves to only one of the current directions, *viz.*, the design of spectrally positioned light sources and give emphasis to materials science-oriented aspects of this problem. A few examples given below will help to outline the current challenges associated with this direction.

Figure 1 depicts a typical IR transmission spectrum of the Earth's atmosphere together with absorption spectra of some molecular gases. It is apparent that the atmosphere has several so-called transmission windows, *i.e.*, spectral ranges of the optical transparency to the electromagnetic radiation. One of such windows is located in the visible region of the spectrum, which is actually a prerequsuite to the existence of life on the Earth. A few of such windows also occur in the IR region of the spectrum, *e.g.*, at 2 – 2.5 μm (5000 – 4000 cm^{-1}) and 4 – 5 μm (2500 – 2000 cm^{-1}). The latter region is of particular interest since it encompasses vibrational features of many molecules, including

T T Basiev, V V Osiko Laser Materials and Technologies Research Centre, A M Prokhorov General Physics Institute, Russian Academy of Sciences, ul. Vavilova 38, 119991 Moscow, Russian Federation.
Fax/tel. (7-495) 135 02 67, e-mail: basiev@lst.gpi.ru (T T Basiev),
tel. (7-495) 135 77 44, e-mail: osiko@lst.gpi.ru (V V Osiko)

Received 28 January 2006
Uspekhi Khimii **75** (10) 939 – 955 (2006); translated by Ya V Zubavichus

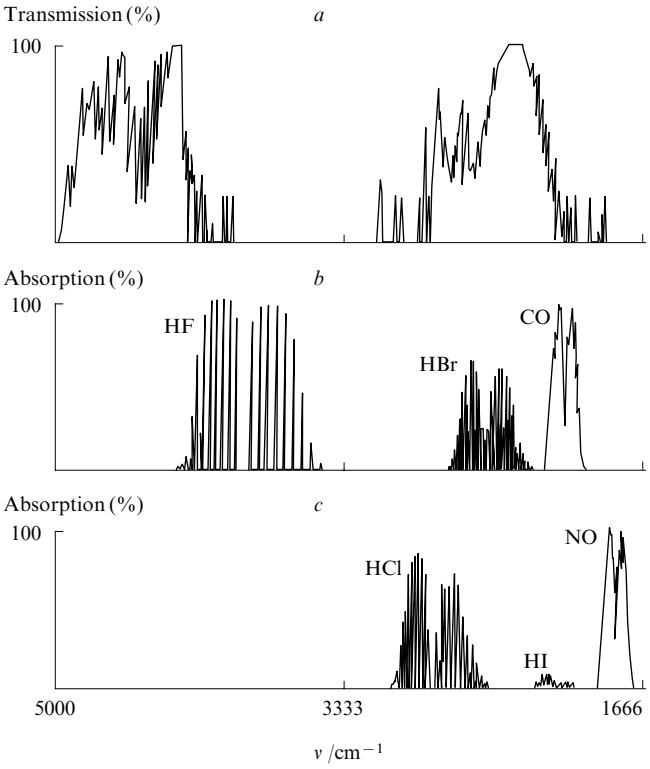


Figure 1. A transmission spectrum of the Earth atmosphere in the IR range (*a*) and IR absorption spectra of some molecular gases (*b*, *c*).[1]

common atmospheric pollutants that are to be controlled, such as hydrogen halides or oxides of carbon, nitrogen and other elements. Remote measurements of the concentration of these molecules in the atmosphere can be accomplished by their excitation with a laser. This requires lasers radiating at strictly defined wavelengths corresponding to the absorption bands of the respective molecules, *i.e.*, spectrally positioned laser sources.

Table 1. Chemical elements possessing useful 'analytical' lines of electronic transitions in the wavelength range of 200–400 nm.[1]

Element	λ_{ex} /nm	λ_{fluor} /nm	Element	λ_{ex} /nm	λ_{fluor} /nm
Ag	328.1	338.3	Ni	301.9	310.1
Al	308.2	308.2	Pb	283.3	405.8
Au	242.8	312.3	Pt	293.0	299.8
B	249.6	249.7	Re	289.6	439.1
Be	234.8	234.8	Sb	231.1	231.1
Cd	326.1	326.1	Se	297.4	534.9
Co	304.4	340.5	Si	251.4	298.8
Cr	335.2	464.6	Sn	286.3	300.9
Cu	324.7	510.5	Sr	293.1	716.7
Fe	296.7	373.5	Ta	287.3	304.9
Ga	287.4	294.4	Te	225.9	253.0
Ge	265.2	275.4	Th	306.0	347.1
Hg	253.6	253.6	Ti	293.3	296.7
In	303.9	329.5	Tl	276.8	352.9
Ir	295.1	322.1	U	311.5	311.5
Li	323.3	323.3	V	283.8	286.4
Lu	298.9	298.9	W	291.1	402.8
Mg	285.2	285.2	Y	297.4	302.2
Mn	279.5	279.5	Zn	307.6	307.6
Mo	294.4	444.3	Zr	296.1	301.1
Nb	374.2	376.4			

Here is another example. The wavelengths of the most intense atomic absorption (λ_{ex}) and fluorescence (λ_{fluor}) lines for a series of common metals are summarised in Table 1. These are the so-called 'analytical' spectral lines suitable for the determination of trace concentrations of these metals using atomic absorption or atomic emission spectroscopy. The remote determination of trace concentrations of metals in the atmosphere, subterranean waters or soils, for instance, for environmental control, also requires spectrally positioned sources but rather in the near UV spectral range.

The list of tasks requiring spectrally positioned sources is rather long. In addition to the aforementioned environmental science, it includes ground-based equipment for the communication with aircrafts and spaceships, fibre-optical communication systems, medicine, *etc*.

Conceptually, the problem of the design of such sources is similar to the problem of the generation and reception of radio waves with a radio receiver strictly tuned to the wavelength emitted by a transmitter. However in the present case, it is the operational frequency of the receiver that is strictly defined and thus the transmitter frequency has to be adjusted accordingly. Besides, modern radio devices allow easy frequency adjustments of the radio signal over a broad range to achieve the resonance. On the other hand, the majority of lasers emit nearly monochromatic radiation at a fixed frequency. Data on the most efficient modern laser crystals are compiled in Table 2. Unfortunately, the 'as is' spectral properties of radiation generated by laser crystals is unsuitable for the design of spectrally positioned radiation sources (since the emission frequencies of these crystals are not resonant will the absorption frequencies of the most convenient receivers). It has to be stressed that spectral lines in the absorption spectra of atoms, ions and molecules are very narrow with typical widths of only $10^{-1}-10^{-2}$ cm^{-1}. The emission spectra of the majority of lasers are similarly narrow ($0.1-1$ cm^{-1}). Therefore, a random exact coincidence of a laser emission frequency and an absorption line of an atom or molecule is of vanishingly low probability.

Table 2. Most popular crystals used in monochromatic lasers.

Crystal	Activator : sensitiser	Oscillation wavelength /μm
$Y_3Al_5O_{12}$	Nd^{3+}	1.064 (0.94; 1.32; 1.444)
	Yb^{3+}	1.030
	Er^{3+}	2.940
	$Ho^{3+}:Tm^{3+}$	2.098
$Gd_3Ga_5O_{12}$	$Nd^{3+}:Cr^{3+}$	1.062
	$Er^{3+}:Cr^{3+}$	2.790
$Y_3Sc_2Ga_3O_{12}$	$Nd^{3+}:Cr^{3+}$	1.058
	$Er^{3+}:Cr^{3+}$	2.791
$Gd_3Sc_2Ga_3O_{12}$	$Nd^{3+}:Cr^{3+}$	1.061
$YAlO_3$	Nd^{3+}	1.079
$KGd(WO_4)_2$	Nd^{3+}	1.067
YVO_4	Nd^{3+}	1.064
$LiYF_4$	Nd^{3+}	1.047 (1.053)

Two major ways to solve the problem of the design of laser sources with strictly spectrally positioned radiation for remote resonant excitation of atomic or molecular systems that are characterised by narrow spectral resonances can be envisaged:

(1) the application of tunable lasers generating light at a variable frequency according to the principle of a transmitter adjustment to resonant absorption frequencies of atoms or molecules;

(2) the conversion of radiation generated by existing lasers by a shift to shorter or longer wavelength ranges to make the spectrum of the transformed radiation match the required wavelength. The radiation of both monochromatic and tunable lasers can be a subject of conversion. A shift in the radiation wavelength

can be achieved with crystals manifesting prominent nonlinear optical properties based on such physical phenomena as harmonic conversion, parametric light generation or stimulated light scattering.

The most promising crystals applicable in tunable lasers and their respective tunability ranges are given in Table 3. It is evident that the frequency tuning can indeed fill up some gaps in the accessible range of laser frequencies, but only to a limited extent.

Table 3. Most popular crystals used in tunable lasers.

Crystal	Activator	Oscillation wavelength range /μm
Al_2O_3	Ti^{3+}	0.650 – 1.110
$Y_3Al_5O_{12}$	Cr^{4+}	1.340 – 1.570
Mg_2SiO_4	Cr^{4+}	1.130 – 1.367
$LiSrAlF_6$	Cr^{3+}	0.780 – 0.990
	Ce^{3+}	0.285 – 0.315
MgF_2	Co^{2+}	1.550 – 2.300
ZnSe	Cr^{2+}	2.200 – 2.812
LiF	F_2^- (see [a])	1.060 – 1.300
	F_2^+ (see [a])	0.800 – 1.100

[a] *F* colour centre.

A significant extension of the accessible range of frequencies has recently been achieved owing to the discovery of materials capable of changing the laser frequency through the stimulated Raman scattering.

II. The laser wavelength conversion using stimulated Raman light scattering

1. Theoretical fundamentals of the purposeful search for efficient materials

The phenomenon known nowadays as Raman light scattering was discovered in 1928. It was independently observed by Raman and Krishnan in liquids [2] and by Landsberg and Mandelshtam in crystals.[3] Essentially, this phenomenon consists of the generation of a secondary radiation shifted to longer wavelengths by a value corresponding to the energy required to excite vibrations of atoms or molecules upon the propagation of an intense monochromatic light beam in a transparent medium. The Raman scattering event can be conveniently considered as a two-photon resonance achieved when the difference between the frequencies of incident (ν_I) and scattered (ν_S) light becomes equal to the frequency of an atomic or molecular vibration in the medium (ν_R)

$$\nu_I - \nu_S = \nu_R .$$

Due to the two-photon nature of the process, its cross-section (σ) is extremely small, *i.e.*, of the order of 10^{-30} cm^2. That is the reason, why light sources with ultimately high radiation spectral densities are necessary for the observation of Raman scattering.

In 1962, Woodbury and Ng [4] observed an intense IR component shifted by 1345 cm^{-1} with respect to the incident light in experiments on the ruby laser light modulation with a nitrobenzene-filled Kerr cell. Later on, this effect was interpreted as the stimulated Raman scattering (SRS).[5]

According to the quantum theory,[5,6] the SRS intensity (associated with the Stokes scattering, *i.e.*, scattering accompanied by a shift to the IR spectral range) is proportional to the density of occupied states corresponding to three interacting fields, *viz.*, laser pumping photons (N_l), photons of the generated scattered wave (N_S) and ground-state phonons (or, equivalently, molecular vibrations) of the crystal (N)

$$\frac{dN_S}{dz} \sim N_l N_S N$$

(z is a coordinate).

In a steady-state mode where the duration of the incident laser pulse is longer than the vibrational phase relaxation time of the medium ($\tau_p \gg T_R$), the SRS intensity (I_S) generated in a layer of a scattering medium with a thickness l is given by

$$I_S(l) = I_S(0)\exp(g_{st} I_l l), \quad (1)$$

where I_l is the incident light intensity, g_{st} is the steady-state-mode gain coefficient

$$g_{st} = \frac{(d\sigma/d\Omega)\lambda_l \lambda_S^2 N}{\pi c \hbar n_S^2 \Delta\nu_R} .$$

Here, $d\sigma/d\Omega$ is the integral scattering cross-section, c is the speed of light, n_S is the refraction index of the medium at the scattered light wavelength, $\Delta\nu_R$ is the width of the respective line in the Raman spectrum.

Therefore, in a steady-state mode, the gain coefficient g_{st} is directly proportional to the integral Raman scattering cross-section and inversely proportional to the width of the respective Raman transition. The line width is, in turn, governed by the mechanism of the vibrational phase relaxation in the medium.[7] The product $\Delta\nu_R^{-1} d\sigma/d\Omega$ quantifies the scattering amplitude in the spectral maximum. Hereinafter, this parameter is referred to as the peak Raman scattering cross-section and denoted as Σ_{peak} .

Wang considered [8] the so-called transient Raman light scattering occurring when $\tau_p \leqslant T_R$ and the pumping spectral width is larger than $\Delta\nu_R$. Under these conditions in the case of a rectangular-shaped pumping pulse, the transient SRS gain coefficient g_{tr} relates to the above parameters through the following expression

$$g_{tr}\, l \approx 2(g_{st} l c \Delta\nu_R \tau_p)^{1/2}.$$

It is apparent from this expression that g_{tr} depends on the pumping pulse duration τ_p and $g_{st}\Delta\nu_R$ product, which represents the integral Raman scattering cross-section. Furthermore, Wang suggested [8] a more straightforward relation of the gain coefficient to fundamental properties of the material. The SRS intensity in the analytical form is given by the following expression

$$I_S(l) \sim I_S(0)\exp\left[2\left(\frac{I_l \tau_p l\, 8\pi^2 c^2 N}{\hbar\omega_S^3 n_S^2}\frac{d\sigma}{d\Omega}\right)^{1/2}\right].$$

As follows from this equation, the SRS gain coefficient is proportional to square root of the integral Raman scattering cross-section $d\sigma/d\Omega$. In this case, the SRS amplification can be estimated from the integral intensity of the respective line in the spectrum of spontaneous Raman scattering

$$\Sigma_{int} \sim \frac{d\sigma}{d\Omega} .$$

This implies that the performace of a material as regards the efficiency of the SRS conversion of the laser radiation can be evaluated based on an analysis of the respective spontaneous Raman scattering spectra. Importantly, such measurements can be performed not only for bulk optically homogeneous species but also for fine polycrystalline powders, which greatly simplifies their experimental realisation.

2. Performance of various inorganic crystals in SRS lasers as estimated by spontaneous Raman light scattering

According to theoretical calculations, the SRS threshold corresponding to $I_S \approx I_l$ is achived at an exponent argument in the formula (1) of ~ 30. Typical values of g_{st} for gaseous and liquid

media lie in the range of 1–3 cm GW^{-1} (*e.g.*, g_{st} = 1.5 cm GW^{-1} and 3 cm GW^{-1} for hydrogen and nitrobenzene, respectively). This implies that the realisation of the SRS mode in these systems requires either a thick scattering medium layer (30–100 cm) or a highly intense ($\sim$1 GW cm^{-2}) pumping radiation.

Among potential media for the SRS conversion of the laser radiation, solid systems and crystals in particular exhibit the following clear advantages:

— a high concentration of Raman-active sites, $N = 10^{22}-10^{23}$ cm^{-3};

— a high gain coefficient, g = 1–50 cm GW^{-1};

— a small scattering length (thin layers of a scattering medium), 1–10 cm;

— a variety of possible Raman shifts, from 10 cm^{-1} to 2000 cm^{-1};

— a broad optical transparency range, from 0.2 μm to 100 μm;

— a high heat conductivity, 1–20 W (cm K)$^{-1}$;

— a weak temperature dependence of the refraction index n, $dn/dT = 10^{-6}-10^{-5}$ deg^{-1};

— a resistivity towards adverse ambient conditions;

— a high thermal stability.

The first observation of the SRS in solids dates back to 1963. Eckhardt *et al.*[9] investigated this effect in crystals of diamond, calcite and α-sulfur. Naturally occurring calcite $CaCO_3$ is a very common SRS material, since it typically forms large single crystals characterised by a relatively high optical homogeneity. Calcite reveals an intense quasi-molecular SRS-active vibrational mode at 1086 cm^{-1} with a width of $\sim$1.2 cm^{-1}. The SRS gain coefficient is 5.5 cm GW^{-1} at an incident wavelength of 532 nm. Diamond crystals are characterised by a record high gain coefficient and a large Raman shift (1332 cm^{-1}) but are of low practical importance due to their small sizes and high costs. In 1980, crystals of metal nitrates, *i.e.*, $NaNO_3$, $Ba(NO_3)_2$ and $Pb(NO_3)_2$, were proposed as promising candidates for observation of the SRS effect.[10] These materials reveal intense vibrational modes at $\sim$1050 cm^{-1} due to the internal totally symmetric vibrations of the quasi-molecular NO_3 groups. The gain coefficient of $Ba(NO_3)_2$ is 47 cm GW^{-1} at an excitation wavelength of 532 nm.[11] With these crystals, the conversion efficiency of the incident laser radiation as high as 80% was achieved at a duration of the laser pulse of a few nanoseconds.[7, 12, 13] Owing to this high efficiency, a number of commercial solid-state SRS lasers were designed based on the $Ba(NO_3)_2$ crystals, in particular, those operating in a spectral range of $\sim$1.5 μm, which is safe for human eyes. However barium nitrate performs well only for the conversion of nanosecond laser pulses. Upon a transition to shorter, picosecond, pulses, the performance of $Ba(NO_3)_2$ is drastically decreased: the SRS threshold is increased by one order of magnitude due to slow relaxation of the vibrational excitations therein ($\sim$30 ns).[14] In addition, $Ba(NO_3)_2$ is characterised by a low moisture resistance, poor heat conductivity and moderate mechanical properties.

Andryunas *et al.*[15] and Basiev *et al.*[16] observed the SRS activity in $KGd(WO_4)_2$ (potassium gadolinium tungstate, hereinafter, referred to as KGW) crystals. The SRS gain coefficient of this tungstate at an incident wavelength of 1064 nm is twice lower than that of $Ba(NO_3)_2$ (6 cm GW^{-1}). Nevertheless, owing to a higher integral gain coefficient, KGW crystals are highly efficient in ps-pulsed SRS lasers.[17] Furthermore, in contrast to nitrates, KGW is characterised by a substantially higher hardness and chemical stability and is relatively inexpensive and available as large single crystals.

Over the last decade, hundreds of crystalline compounds belonging to different classes have been evaluated and compared in the Laser Materials and Technologies Research Centre at the A M Prokhorov General Physics Institute of the Russian Academy of Sciences. The classes of compounds studied include metal and ammonium carbonates, nitrates, phosphates, borates, silicates, niobates, chlorates, bromates, iodates, sulfates, molybdates and tungstates. As a basic method for the preliminary evaluation of crystals under study, spontaneous Raman light scattering was utilised.[16, 17]

An Ar ion laser operated at a wavelength of 488 nm was used as a radiation source in Raman scattering experiments. The power of the laser beam at a sample surface was 1 W. The Raman scattering spectra were acquired with a Spex Ramalog-1403 double spectrometer in the backscattering geometry. The spectral resoultion of the setup was 0.2–1.0 cm^{-1}. Both single crystals and polycrystalline powders were investigated. For a correct comparison of the integral and peak scattering cross-sections among different samples, the measurements were performed on rectangular plates with thicknesses of 0.7 mm or 2 mm cut from the respective single crystals. A plate with a thickness of 0.7 mm cut from a diamond crystal was used as an intensity reference. The intensity of the laser radiation and slit settings of the spectrometer were kept constant throughout the measurements. In order to study the orientational effects, the measurements were performed at different crystallographic orientations of the samples relative to the polarisation plane ($\boldsymbol{E}$) of the incident laser radiation. The as-measured Raman spectra were processed with a specialised software code to retrieve line widths as well as peak and integral scattering cross-sections. The accuracy of the line width determination, which is determined by the spectral resolution of the setup, was $\sim$10% for moderately broad ($\Delta\nu_R > 1$ cm^{-1}) lines. The peak scattering cross-sections Σ_{peak} were determined to within $\sim$10% and $\sim$20% for broad and narrow lines, respectively. The accuracy of the Σ_{int} determination is estimated as 10% and 20%–40% for narrow and broad lines, respectively.

Results of the measurements are compiled in Table 4. The values of Σ_{int} and Σ_{peak} for all materials are scaled to those of diamond, since diamond is characterised by one of the most intense Raman lines. As has been discussed above, the integral Raman scattering cross-section determines the SRS gain coefficient in a transient mode. According to the tabulated data, large Σ_{int} are observed, apart from diamond, for lithium niobate (166%) for a vibrational mode at 632 cm^{-1}, various molybdates and tungstates (from 46% to 65%) and lithium iodate (54%). Smaller integral Raman scattering cross-sections are typical of sodium and barium nitrates (23% and 21%, respectively), calcite (6%), calcium and strontium fluorapatites (3.4%) and quartz (2.2%). All molybdates and tungstates studied can be subdivided into two groups based on their crystal structures: compounds with the scheelite ($CaWO_4$) structure corresponding to the tetragonal space group C_{4h}^6 and monoclinic structures characterised by the space group C_{2h}^6. For the first group of crystals, intense Raman scattering lines are attributed to totally symmetric vibrations of the WO_4 tetrahedra. For the second group of compounds, the two intense lines observed in the Raman spectra are attributed to vibrations of the W–O bonds in the WO_6 octahedra.[18]

Meanwhile, the SRS amplification in a steady-state mode is determined by the peak scattering cross-section Σ_{peak}. According to the experimental data in Table 4, a large gain is expected for diamond and sodium and barium nitrates. Because of very narrow Raman lines, crystals of $Ba(NO_3)_2$ and $NaNO_3$ manifest large values of Σ_{peak}, despite the fact that the integral cross-sections corresponding to their SRS-active vibrational modes are 2–3 times smaller than those of tungstates. Accurate measurements[19, 20] afforded the record small line width of $\sim$0.4 cm^{-1} for $Ba(NO_3)_2$, which is severalfold smaller than that for diamond. The peak cross-section Σ_{peak} of this Raman mode in $Ba(NO_3)_2$ amounts to 63% of the respective diamond value and is more than twice larger than that in KGW crystals. In the case of $NaNO_3$, Σ_{peak} is only 44% due to the larger line width ($\sim$1 cm^{-1}) Lithium iodate and monoclinic tungstates are characterised by moderately broad Raman lines (5–8 cm^{-1}) and relatively large peak cross-sections ranged from 10% to 35%. A Raman mode of lithium niobate at 632 cm^{-1} is significantly broader (27 cm^{-1}) but is characterised by a relatively large peak cross-section Σ_{peak} (18%)

Table 4. Basic Raman parameters of crystals of inorganic compounds.

Crystal	Space group	Molecular group	Raman frequency /cm^{-1}	Raman line width /cm^{-1}	Σ_{int} (%)	Σ_{peak} (%)
Diamond	O_h^7	–	1332.9	2.7	100	100
Simple oxides						
SiO_2	D_3^6	SiO_4	464	7	2.2	1.2
TeO_2			648	9	150	32
Nitrates and carbonates						
$Ba(NO_3)_2$	T_h^6	NO_3	1048.6	0.4	21	63
$NaNO_3$	D_{3d}^6	NO_3	1069.2	1.0	23	44
$CaCO_3$	D_{3d}^6	CO_3	1086.4	1.2	6.0	10.6
Tungstates						
$CaWO_4$	C_{4h}^6	WO_4	910.7	6.95	50	18.6
$SrWO_4$	C_{4h}^6	WO_4	921.5	3	50	41
$BaWO_4$	C_{4h}^6	WO_4	926.5	1.63	52	64
$NaGd(WO_4)_2$	C_{4h}^6	WO_4	919	14	–	–
$NaY(WO_4)_2$	C_{4h}^6	WO_4	918	15	–	–
$Sc_2(WO_4)_3$	–	WO_4	1024	15	–	–
$In_2(WO_4)_3$	–	WO_4	1023	13	–	–
$LiIn(WO_4)_2$	–	WO_4	920	8	–	–
Na_2WO_4	O_h^7	–	929.2	1.8	–	–
$KGd(WO_4)_2$	C_{2h}^6	WO_6	901	5.4	50	35
$KY(WO_4)_2$	C_{2h}^6	WO_6	905.6	7	46	35
$KYb(WO_4)_2$	C_{2h}^6	WO_6	908	7.4	48	34
Molybdates						
$CaMoO_4$	C_{4h}^6	MoO_4	879.3	5.0	65	34
$SrMoO_4$	C_{4h}^6	MoO_4	887.7	2.8	63	51
$BaMoO_4$	C_{4h}^6	MoO_4	892.4	2.1	55	64
Iodates and niobates						
$LiIO_3$	C_6^6	IO_3	821.6	5.0	54	25
$LiNbO_3$	C_{3v}^6	NbO_6	872	21.4	44	5
	C_{3v}^6	NbO_6	632	27	166	18
$LaNbO_4$	C_{2h}^3	NbO_4	805	9	22	7.1
Phosphates						
$Ca_5(PO_4)_3F$	C_{6h}^2	PO_4	964.7	2.8	3.4	3.8
$Sr_5(PO_4)_3F$	C_{6h}^2	PO_4	950.3	2.8	3.4	3.8
Li_3PO_4	–	PO_4	951	7.7	–	–
Miscellaneous salts						
$NaClO_3$	–	ClO_3	937	4.9	–	–
$NaBrO_3$	–	BrO_3	799.5	2.5	–	–
NH_4Cl	O_h^1	NH_4	1712	6	–	–

owing to a very large integral cross-section of 166%. A comparable value of Σ_{peak} is observed for crystals of natural calcite (10.6%). $CaWO_4$ crystals demonstrate a large integral cross-section of 50% but relatively low peak cross-section of 18.6% due to a significant line broadening of 6.95 cm^{-1}. As for $SrWO_4$ and $BaWO_4$, owing to small line widths of 3 cm^{-1} and 1.63 cm^{-1}, their peak cross-sections Σ_{peak} amount to 41% and 64%, respectively, which is larger than that in other tungstates and comparable to values typical of nitrates. The highest-frequency Raman lines of lanthanum and lithium niobates (at 805 cm^{-1} and 872 cm^{-1}, respectively) are characterised by relatively low Σ_{peak} values of 7.1% and 5%, respectively. Calcium and strontium fluorapatites reveal even higher-frequency lines but smaller Σ_{peak} values of 3.8%. All these values are small but nevertheless close to the respective Σ_{peak} value of calcite, which is used for the SRS generation on a commercial basis both with ns- and ps-pulsed lasers.

Due to the large Raman shifts (800–960 cm^{-1}) and broad lines ($\Delta\nu_R$ = 3–20 cm^{-1}), the crystals of aforementioned niobates and apatites can prove useful for SRS in the picosecond range.

Other materials listed in Table 4 exhibit small peak Raman scattering cross-sections. Notwithstanding, they still can be useful, since they provide different Raman shifts.

Therefore, the above comparative analysis of the SRS-active modes for various crystalline materials based on their spontaneous Raman scattering spectra indicates that calcite and sodium and barium nitrates should provide large SRS gain coefficient in a steady-state mode for nanosecond pulses. A shortening of pumping pulses to 20–30 ps switches the SRS mode to a transient one, which gives rise to a substantial increase in the SRS threshold for these crystals. A more efficient SRS generation at shorter pumping pulses can be achieved with tungstate crystals, which are characterised by relatively broad Raman lines. Due to the large integral cross-sections, these crystals are expected to perform well

in a transient SRS mode. Due to their outstanding spectroscopic properties, $SrWO_4$ and $BaWO_4$ crystals are capable of providing high SRS gain coefficients both for ns- and ps-pulsed lasers, which substantiates their great potential as versatile nonlinear optical media for the highly efficient SRS-based frequency converters. It is also of note that, in addition to tungstates, molybdates demonstrate very attractive SRS properties.

III. The preparation and characterisation of single crystals of calcium, strontium, barium and lead molybdates and tungstates for SRS lasers

Caclium, strontium, barium and lead molybdates and tungstates represent congruently melting compounds having no (except for $BaMoO_4$) phase transitions over the entire temperature range from room temperature to the melting point. Single crystals of these compounds can be grown by melt crystallisation. Their melting points lie below 1535 °C and thus platinum crucibles can be used for crystal growth. Platinum is characterised by a melting point of 1770 °C, and platinum crucibles can be used in air. Most typically, crystals of molybdates and tungstates are grown by the so-called Czochralski method based on a slow pulling of a crystal growing on a seed from the respective melt.[21] Ivleva *et al.*[22] reported on the growth of single crystals of some tungstates by the modified Stepanov method based on the use of a bulk shaper.

Below we consider in more details the growth of barium tunstate crystals by the Czochralski and Stepanov methods. Barium tungstate crystallise in the tetragonal scheelite structure and has a melting point of 1475 °C. Single crystals of this compound were grown on a Kristall-3M crystal-growth furnace equipped with an inductively heated platinum crucible with a melt. Starting $BaWO_4$ was prepared by sintering of $BaCO_3$ and WO_3 of the purity grade 5N taken in a stoichiometric ratio. The seed was oriented along the [100] direction. The crystalliser is schematically depicted in Fig. 2. A cylindrical platinum screen was placed above the crucible to prevent overheating of the crucible walls and reduce temperature gradients along the growing crystal. The axial temperature gradient was kept in a range from 50 to 100 °C per cm, while the radial temperature gradient was fixed at ~5 °C per cm. High optical-quality crystals were grown at a pulling rate of 2–6 mm h^{-1} upon a constant rotation at 30 rpm. An excess of WO_3 of 0.5 mass % – 1.2 mass % was added to the melt to suppress emergence of light-scattering inclusions in the crystals.

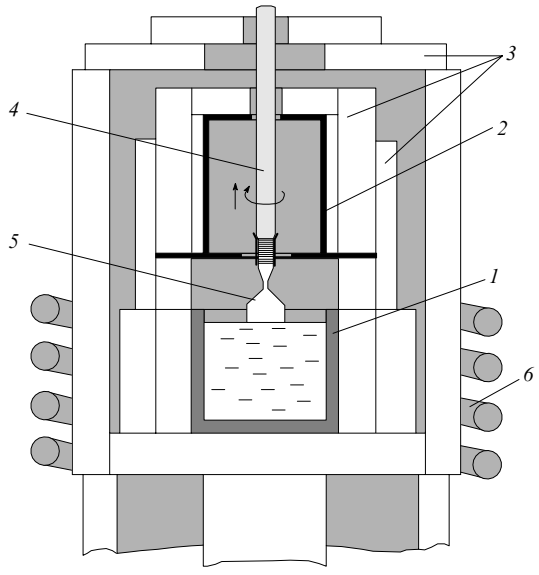


Figure 2. A scheme of the crystalliser furnace used for crystal growth of calcium, strontiun, barium and lead molybdates and tungstates using the Czochralski method.
(*1*) Platinum crucible, (*2*) platinum thermal shield, (*3*) heat-insulating elements made from corundum ceramics, (*4*) seed holder, (*5*) growing crystal, (*6*) RF heater.

The crystalliser used for crystal growth by the modified Stepanov method is schematically depicted in Fig. 3. According to this method, a special platinum shaper is plunged into the melt. The melt from the crucible is supplied through the feeding capillaries of the shaper to a thin layer of the melt in the contact with the crystal growth front. The thickness of the contact melt layer is controlled by the temperature of the crucible and the position of the shaper relative to the crucible. Meanwhile, the shape of the crystallisation field and the cross-section of the growing crystal are determined by the shaper profile. A crystal is grown on a seed, typically, without rotation. The growth process can be optimised by varying the shaper design and temperature gradients. The growth of specifically shaped crystals has some distinctive features related to their structures. In particular, the anisotropy of growth rates of different crystallographic faces has to be taken into account. According to the Curie principle, in the case of $BaWO_4$ that crystallises in the tetragonal space group C_{4h}^6, the crystallographic *a* axis is the preferable growth direction and a rectangle is the preferable contact surface of the shaper.

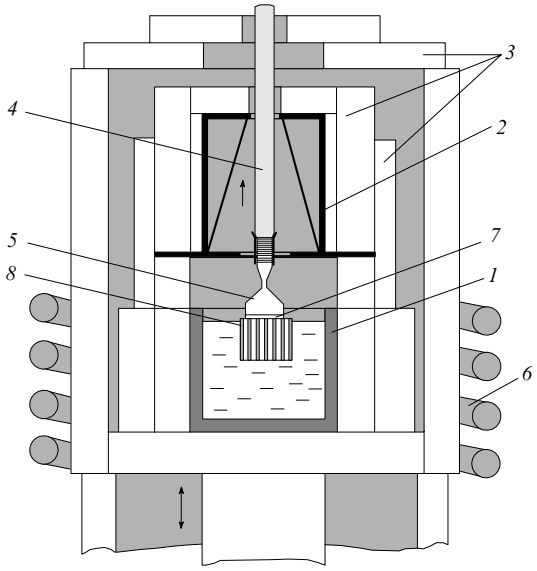


Figure 3. A scheme of the crystalliser furnace used for crystal growth of calcium, strontiun, barium and lead molybdates and tungstates using the modified Stepanov method.
(*1*) Platinum crucible, (*2*) platinum thermal shield, (*3*) ceramic heat-insulating elements, (*4*) rod made from leucosapphire, (*5*) growing crystal, (*6*) RF heater, (*7*) meniscus of the melt, (*8*) shaper.

Photographic images of the tungstate crystals grown by both methods are shown in Fig. 4.

Laser devices place extremely strong requirements on the quality (optical perfection) of materials to be used as working media.[23] Such crystals and glasses should contain no solid or gaseous inclusions, domain boundaries and cracks. Refraction index gradients of a medium should not exceed 10^{-4}–10^{-6} cm^{-1}. The presence of any of these defects in an optical medium gives rise to efficiency losses (due to light scattering on optical inhomogeneities) and radiation damage of the material. Consequently, such materials are unsuitable for the practical use. The above requirements are even stricter for

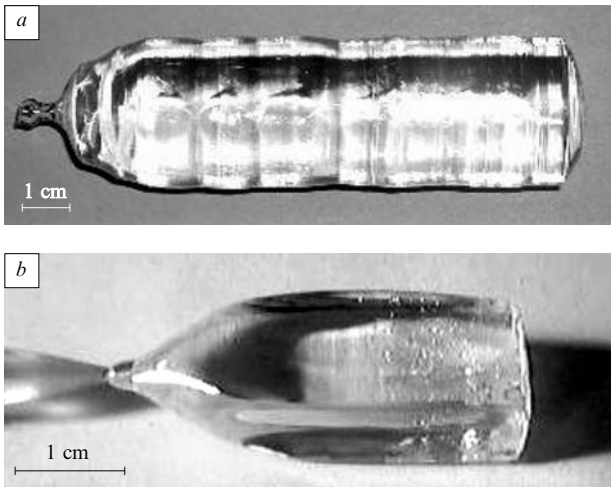


Figure 4. Photographic images of $BaWO_4$ crystals grown from melts using the Czochralski method at a pulling rate of 2–6 mm h^{-1}, a rotation rate of 30 rpm and a volume growth rate of < 1 cm^3 h^{-1} upon an excess of WO_3 in the melt of 1 mass % – 1.5 mass % (*a*) and using the modified Stepanov method at a pulling rate of 5 mm h^{-1} (no rotation) and a volume growth rate of 0.5 cm^3 h^{-1} upon an excess of WO_3 in the melt of 1 mass % (*b*).[22, 23]

potential SRS crystals, which often operate at ultimately high laser radiation intensities of the order of $10^8 - 10^9$ W cm^{-2}.

The crystal growth by the Czochralski method can produce the following specific defects intrinsic to the method:

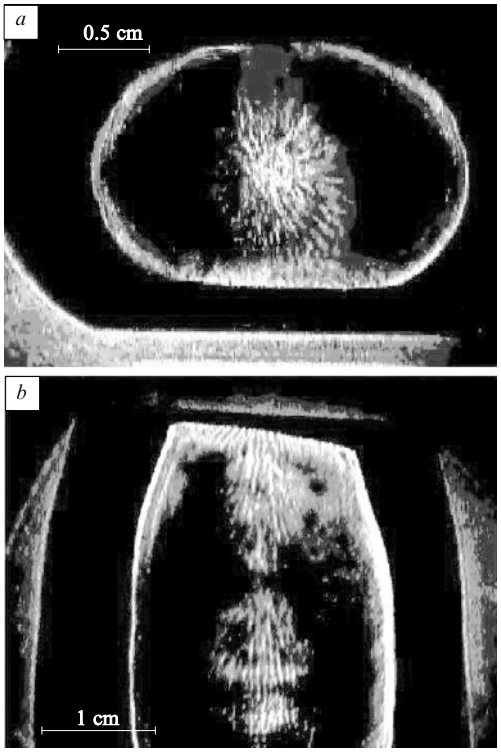


Figure 5. A typical central defect (a 'core') in a $BaWO_4$ single crystal grown by the Czochralski method.[22, 23]
(*a*) A cross-section perpendicular to the growth axis, *a*; (*b*) a cross-section parallel to the growth axis, *a*.

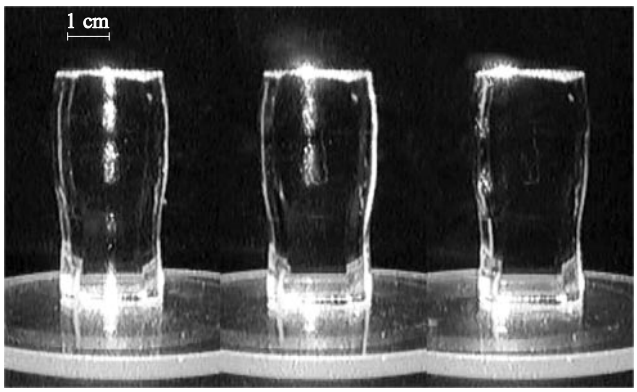


Figure 6. Microscopic inclusions of a foreign phase in a $BaWO_4$ single crystal grown by the Czochralski method (observation in a laser beam).[22, 23]

— 'a core', *i.e.*, a central part of the crystal in the form of a core defect going along the entire crystal from bottom to top; the emergence of this defect relates to the face growth from the cone vertex at the interface between solid and liquid phases (Fig. 5);

— growth striations;

— microscopic inclusions of foreign phases (Fig. 6);

— cracks along the cleavage planes of a crystal.

In order to prevent or suppress the formation of a 'core', the growth front has to be the least convex or ideally flat. This can be achieved by a decrease in both the vertical temperature gradient along the crystal and the radial temperature gradient across the crystallisation front.

Growth striations occur as a result of a periodically inhomogeneous distribution of the main crystal components or admixtures due to variations in the growth rate. Typically, elimination of possible factors responsible for these variations, such as instabilities of pulling of the crystal and rotation mechanisms or fluctuations in the temperature of the melt, minimises this defect.

Tungstate crystals grown from exactly stoichiometric melts often contain microinclusions of foreign solid phases, which cause opalescence of crystals. These defects are attributed to a violation of the melt stoichiometry in the course of crystal growth due to progressive evaporation of tungsten trioxide. The use of a small excess of WO_3 (up to 1.5 mass %) in the furnace charge makes it possible to avoid the emergence of such light-scattering inclusions. Alternatively, optically homogeneous tungstates can be grown by the addition of $\sim$0.5 mass % rare-earth metal oxides (La_2O_3, Nd_2O_3, *etc.*) to the melt for the crystal growth.

The specific defects in $BaWO_4$ crystals grown by bulk shaping methods include cracks along certain crystallographic directions, in particular, parallel to [001] and light-scattering micro- and macroinclusions. The use of exactly stoichiometric melts and too high pulling rates increases the probability of the appearance of inclusions. In this method of crystal growth, the shape of the crystallisation front is strongly dependent on the design of the shaper. The flatness of the crystallisation front is violated in the case of shapers with excessively wide slits (Fig. 7). This gives rise to crystals with a prominent domain structure and, consequently, abundant cracks. Ivleva *et al.*[22] utilised shapers with capillary slits of 1 mm and 0.1 mm. In the latter case, the crystallisation front was nearly flat, which afforded highly homogeneous crystals.

The use of smaller temperature gradients also improves the optical homogeneity of the resultant crystals. In the growth experiments, platinum crucibles with diameters from 40 mm to 80 mm were tested. It is known that an increase in the crucible size and, respectively, in the melt volume decreases the temperature gradients, which gives rise to larger and higher-quality crystals.

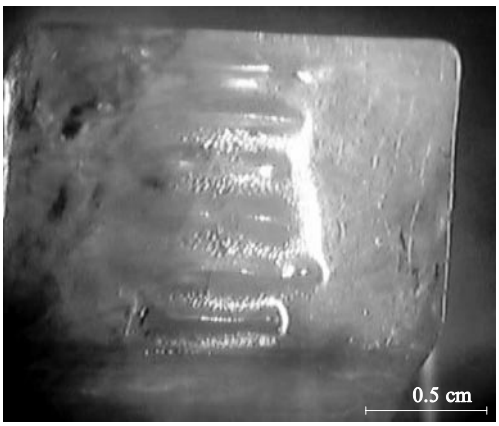


Figure 7. The crystallisation surface of a $BaWO_4$ single crystal grown by the modified Stepanov method with a shaper having slits with a thickness of 1 mm.[22,23]
The intergrowth of the crystal into the capillary slits can easily be seen.

The optimum conditions for the growth of tungstate crystals were found to be: the pulling rate of 1–5 mm h^{-1} at a volume growth rate no faster than 0.5 cm^3 h^{-1}, the capillary slit width (if a shaper is used) of 0.1–0.2 mm, the excess of WO_3 in the melt of 1 mass %, the axial temperature gradient of 50 °C per cm. Under these or similar conditions, optically homogeneous crystals of calcium, strontium, barium [22,24–26] and lead [27] molybdates and tungstates with sizes of 30×100 mm were successfully grown.

IV. Raman scattering spectra of calcium, strontium, barium and lead molybdates and tungstates

As has been discussed above, crystals of molybdates and tungstates are characterised by similar integral scattering cross-sections, whereas the widths of the respective spectral lines are substantially different. It is the line width that determines the peak scattering cross-section provided that the integral cross-sections are almost identical. Furthermore, the value of the Raman shift strongly varies in a series of molybdates and tungstates. It is necessary to correlate these parameters with the chemical composition and crystal structure in order to enable the prediction of Raman scattering and SRS effects and purposeful search for novel efficient SRS-based laser converters. These issues are considered in detail elsewhere.[26] The spectra of spontaneous Raman light scattering were measured for an extended series of molybdates $MMoO_4$ and tungstates MWO_4 (M = Ca, Sr, Ba, Pb, Zn). The vast majority of samples for measurements were prepared as bulky single crystals. Only $ZnMoO_4$ and $ZnWO_4$ were obtained as polycrystalline ceramic specimens by sintering of thoroughly mixed zinc carbonate with either MoO_3 or WO_3 at 1100–1200 °C. The sample plates were cut from the single crystals either parallel or perpendicular to the crystallographic c axis upon the determination of the orientation by X-ray diffraction.

Raman spectra were excited with Ar laser radiation with $\lambda = 488$ nm and registered using a Spex Ramalog-1403 spectrometer at 77 K and 300 K. High-temperature Raman spectra (up to 1920 K) were measured using an original method described elsewhere.[28] Excitation was achieved with a pulsed Cu vapour laser operated at a wavelength of 501.5 nm and a pulse repetition rate of 10 kHz. The spontaneous Raman scattering spectra were recorded using the time-resolved technique, which provides a high signal-to-thermal background ratio. High-temperature Raman spectroscopy is indispensable in studies of solid-state phase transitions; additionally, it yields important information on positions and widths or Raman lines as a function of the temperatue up to and above the melting point.

First measurements of room-temperature spontaneous Raman scattering spectra of calcium, strontium and lead molybdates and tungstates date back to the mid-1960s.[29] Meanwhile, barium molybdate and tungstate spectra remained unstudied. All the above molybdates and tungstates except for zinc compounds crystallise with the scheelite structure corresponding to the tetragonal space group C_{4h}^6. A primitive unit cell contains two formula units. The Mo–O and W–O bonds in the quasi-molecular tetrahedral $[MoO_4]^{2-}$ and $[WO_4]^{2-}$ anions are essentially covalent, and the anions are only weakly bound to the M^{2+} cations. With this regard, features in the Raman spectra of these crystals can be subdivided into two groups, *viz*., internal and external vibrational modes. The internal vibrations include totally symmetric vibrations of the oxygen atoms relative to the central Mo or W atom, *i.e*., the so-called breathing modes. The external (or lattice) phonons correspond to vibrations of the M^{2+} ions relative to rather rigid quasi-molecular $[MoO_4]$ and $[WO_4]$ groups. Free MoO_4 and WO_4 tetrahedra are characterised [29] by the point symmetry T_d. According to the group theory, 15 degrees of freedom are possible in this symmetry group, which can be classified into four internal vibrational [$\nu_1(A_1)$, $\nu_2(E)$, $\nu_3(F_2)$ and $\nu_4(F_2)$], one rotational [$\nu_{fr}(F_1)$] and one translational (F_2) modes. When $[MoO_4]$ or $[WO_4]$ groups are placed into the scheelite lattice, the crystal-field symmetry is lowered to S_4. This gives rise to splitting of all degenerate vibrations due to the crystal field effects.[29] Furthermore, the presence of two formula units in a unit cell gives rise to an additional, the so-called Davydov, splitting (DS) of the vibrational modes. For instance, the $\nu_1(A_1)$ and $\nu_3(F_2)$ vibrational modes of a free tetrahedral group are split in the scheelite crystal field in the following way:

$$\nu_1(A_1) \longrightarrow \nu_1(A) \longrightarrow \nu_1(A_g) + \nu_1(B_u),$$

$$\nu_3(F_2) \longrightarrow \nu_3(E) + \nu_3(B) \longrightarrow \nu_3(E_g) + \nu_3(E_u) + \nu_3(B_g) + \nu_3(A_u).$$

Calculations within the group theory gives 26 different vibrations

$$\Gamma = 3A_g + 5A_u + 5B_g + 3B_u + 5E_g + 5E_u \qquad (2)$$

corresponding to the wavevector $\boldsymbol{K} = 0$. All gerade vibrations (*i.e*., $3A_g$, $5B_g$ and $5E_g$) are Raman-active, whereas the ungerade modes (*i.e*., $4A_u$ and $4E_u$) can only be observed in IR absorption spectra. Three B_u vibrations represent the so-called silent modes. Two acoustic vibrations, A_u and E_u, also occur in the expression (2).

The Raman spectra measured by Basiev *et al*. [26] agree well with the earlier reported data.[29,30] The spectra of $BaMoO_4$ and $BaWO_4$ crystals studied for the first time are shown in Fig. 8. The results of spectra processing are collected in Table 5. The $BaWO_4$ crystals retain the scheelite structure over the entire temperature range from room temperature to the melting point. Meanwhile, it was found that $BaMoO_4$ undergoes a phase transition at 1600 K from the tetragonal modification (β) into a cubic structure (α). The Raman spectra in Fig. 8 *a* clearly demonstrate that two ν_3 vibrations coalesce and the ν_{ext} band strongly shifts above 1600 K. A comparison of the Raman spectra of $BaMoO_4$ measured at two ultimate temperatures indicates that the crystal-field symmetry experienced by a $[MoO_4]$ group in a melt at 1800 K is nearly the same as that in the crystalline state at 1605 K.

Shifts in the Raman-active frequencies for calcium, strontium, barium and lead molybdates and tungstates as a function of the cation mass and the unit cell parameter c are depicted in Figs 9 and 10, respectively. It is evident that the trends are identical in both series. There are several factors affecting the observed Raman shifts. Kanamory *et al*. [31] suggested that it is the cation mass that is mainly responsible for the frequency of the low-energy external vibration ($2B_g + 2E_g$). This suggestion is supported by a monotonic decrease in the external vibrational frequency ν_{ext} with an increase in the cation mass M (see Fig. 9). However experi-

Table 5. Raman frequencies of $BaWO_4$ and $BaMoO_4$ in the crystalline and molten states.[26]

Irreducible representation of the Raman mode	$BaWO_4$			$BaMoO_4$					Assignment
	300 K (see [a])	1800 K (see [a])	1820 K (see [b])	300 K (see [a])	1600 K (see [c])	1605 K (see [d])	1770 K (see [d])	1800 K (see [b])	
A_g	925	910	909	892	878	877	873	822	$\nu_1(A_1)$
B_g	831	816	804	837	825	802	794	777	$\nu_3(F_3)$
E_g	795	775	–	791	771	–	–	–	
E_g	353	338	370	358	347	359	356	356	$\nu_4(F_2)$
B_g	345	–	0	345	–	–	–	–	
B_g	332	318	326	324	313	313	313	314	$\nu_2(E)$
A_g	332	–	–	324	–	–	–	–	
E_g	191	109	–	188	143	134	–	–	$\nu_{fr}(F_1)$ (rotational mode)
A_g	150	–	–	–	140	–	–	–	
B_g	132	–	–	137	–	–	–	–	ν_{ext} (external modes)
E_g	101	73	–	110	–	–	–	–	vibrations of $[MoO_4]^{2-}$, $[WO_4]^{2-}$ and Ba^{2+}
E_g	75	–	–	74	57	45	–	–	–
B_g	63	58	–	76	73	–	–	–	–

[a] Crystal with the C_{4h}^6 symmetry. [b] Melt. [c] β-Modification with the C_{4h}^6 symmetry. [d] α-Modification with the cubic symmetry.

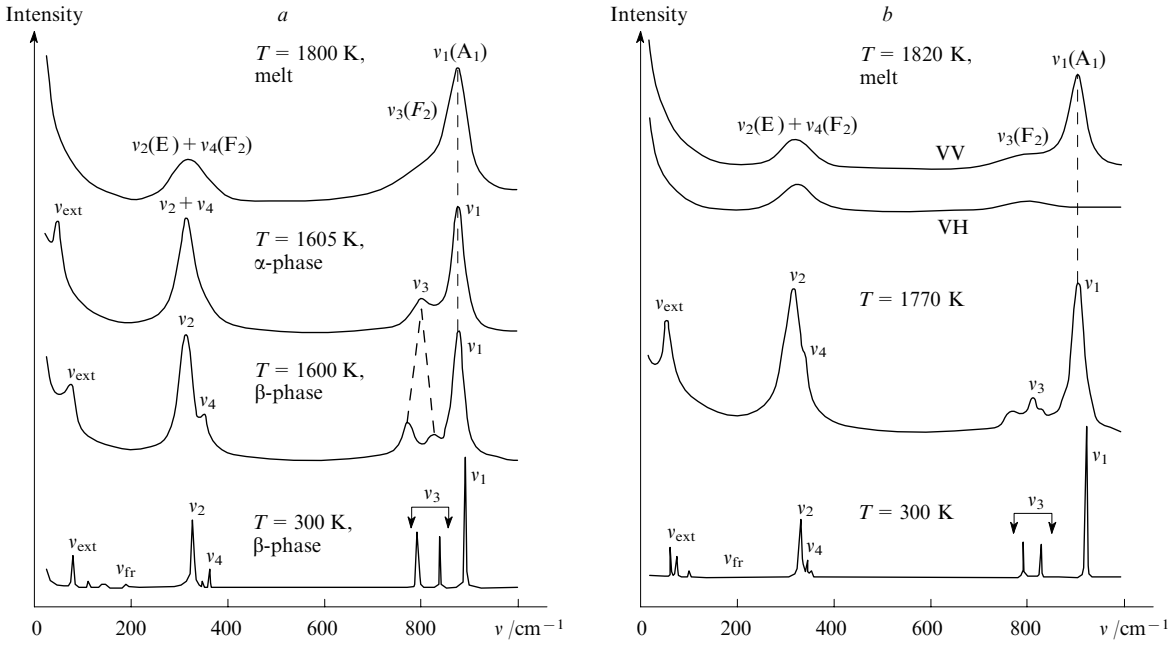


Figure 8. Temperature-dependent non-polarised Raman scattering spectra of $BaMoO_4$ (*a*) and $BaWO_4$ (*b*) in the crystalline and molten states.[26] Here and in other figures, the notation VV (VH) denotes the experimental geometry with the polarisation plane of the scattered beam parallel (perpendicular) to the polarisation plane of the incident beam.

ments showed [26] that the frequencies of the internal vibrational modes of the $[MoO_4]$ and $[WO_4]$ groups [except for the $\nu_2(E)$ doublet] also depend on the cation nature.

One of possible reasons for this effect lies in the fact that an increase in the ionic radii in the Ca–Sr–Ba series gives rise to some dilatation of the unit cell and, subsequently, to a small change in the Mo–O and W–O bond lengths within the tetrahedra. This should also be accompanied by a change in the force constants corresponding to certain internal vibrational modes. Apparently, the unit cell parameters exert the strongest influence on the force constants corresponding to the $\nu_4(F_2)$ and $\nu_{fr}(F_1)$ modes (see Fig. 10). On the other hand, the unit cell parameters of $PbMoO_4$ and $PbWO_4$ are close to those of $SrMoO_4$ and $SrWO_4$ (Table 6) and it seems logical to expect similar internal vibrational frequencies for them. In contrast to these expectations, frequencies of all internal vibrations of $PbMoO_4$ and $PbWO_4$ deviate from the monotonic dependences plotted in Fig. 10. The largest shifts are observed for the high-energy modes, *i.e.*, $\nu_1(A_g)$, $\nu_3(B_g)$ and $\nu_3(E_g)$. This deviation cannot be explained by effects of the unit cell parameters alone. It was suggested that another crystal-chemical factor gets involved, *viz.*, a partially covalent character of the chemical bonds formed by the M^{2+} cations with the oxygen atoms constituting the MoO_4 and WO_4 groups. This factor also affects [32] the force constants of the internal vibrations. A higher electronegativity of an M^{2+} cation gives rise to larger force constants corresponding to centrosymmetric vibrations and, respectively, to higher frequencies of the vibrational modes (see Table 6). Additionally, the formation of

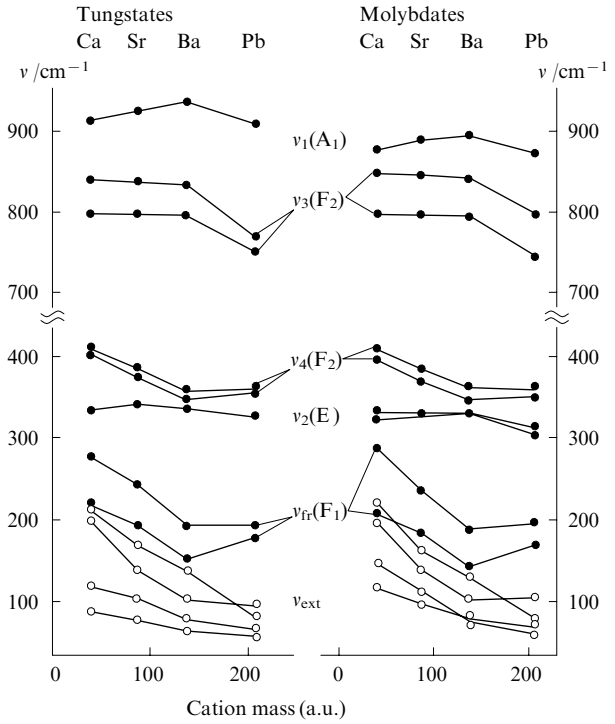


Figure 9. Changes in the Raman frequencies along the $MMoO_4$ and MWO_4 homologous series (M = Ca, Sr, Ba, Pb) as a function of the cation mass M^{2+} (see Ref. 26).

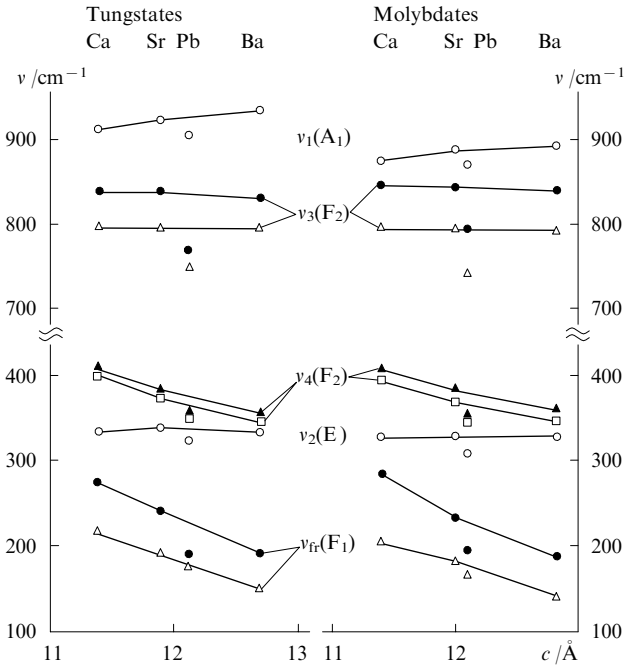


Figure 10. Changes in the the Raman frequencies along the homologous series of calcium, strontium, lead and barium molybdates and tungstates as a function of the unit cell parameter.[26]

partly covalent M–O bonds changes the effective mass of vibrating atomic groups in a way that a reduced mass of the metal–oxygen pair should substitute the mass of a single oxygen atom in the frequency calculations. In this indirect way, the mass of an M^{2+} cation can affect the internal vibrational frequencies of the $[MoO_4]$ and $[WO_4]$ groups. The influence exerted by the nature of an M^{2+} cation on the internal vibrational frequencies is dominantly asribed to the effects of force constants. However Lazarev *et al.*[32] did not specifically address the case of a very heavy cation simultaneously characterised by a high electronegativity, such as Pb^{2+}.

The ambiguity of the above interpretation concerning the dependence of the internal vibrational frequencies on the cation nature relates to the fact that this dependence in real crystals is masked by static crystal-field effects and dynamical coupling of different vibrational modes. The crystal lattice effects can be excluded by measuring Raman spectra in melts of the respective compounds. High-temperature Raman spectra of the melts were measured using the experimental setup described above. The experimental spectra of melts derived from the scheelite-type crystals are fully consistent with the presence of tetrahedral groups with the T_d point symmetry (Fig. 11). They reveal four vibrational modes, *viz.*, $\nu_1(A_1)$, $\nu_2(E)$, $\nu_3(F_2)$ and $\nu_4(F_2)$. The $\nu_1(A_1)$ mode is attributed to totally symmetric vibrations of the oxygen atoms relative to the central atom (Mo or W). In order to monitor the effects of the cation mass on the internal vibrational frequencies, the Raman spectra of $ZnMoO_4$ and $ZnWO_4$ melts were also included into the comparative analysis. Zinc is characterised by

Table 6. Basic Raman parameters and selected crystallochemical characteristics of $Ba(NO_3)_2$, $MMoO_4$ and MWO_4 crystals (M = Ca, Sr, Ba, Pb, Zn).[26]

Crystal	ν (at 300 K) /cm^{-1}	Σ_{int} (%)	Σ_{peak} (%)	$\Delta\nu_R$ /cm^{-1}		Parameters of the M^{2+} cation			Unit cell parameters /Å		ΔE /cm^{-1}	Mo–Mo or W–W distance /Å
				300 K	77 K	m_{cat}	r_{cat} /Å	η_{cat}	c	a		
$Ba(NO_3)_2$	1048	21	63	0.4	0.3	137.34	1.42	0.78	8.11	8.11	< 0.69	–
$BaWO_4$	925	52	64	1.6	0.97	137.34	1.42	0.78	12.720	5.640	0–1	6.95
$SrWO_4$	921	50	41	3.0	1.45	87.62	1.25	1.06	11.921	5.417	28	6.5
$CaWO_4$	911	50	18.6	5.6	3.1	40.08	1.12	1.22	11.376	5.242	58	6.26
$PbWO_4$	905	171	97	4.7	1.87	207.19	1.29	3.08	12.12	5.50	32	6.65
$ZnWO_4$	908	–	–	8.0	5.0	65.38	0.9	2.98	–	–	–	–
$BaMoO_4$	892	55	64	1.85	1.1	137.34	1.42	0.78	12.82	5.62	0–1	7.0
$SrMoO_4$	887	63	51	2.5	1.2	87.62	1.25	1.06	12.02	5.394	22	6.58
$CaMoO_4$	879	65	34	5.5	2.3	40.08	1.12	1.22	11.43	5.266	52	6.28
$PbMoO_4$	871	397	146	8.0	3.2	207.19	1.29	3.08	12.108	5.436	36	6.63
$ZnMoO_4$	971	–	–	–	–	65.38	0.9	2.98	–	–	–	–

Note. The following notations are adopted: m_{cat} is the atomic mass (a.u.); r_{cat} is the ionic radius; η_{cat} is the electronegativity; ΔE is the Davydov splitting. The electronegativities values used in this table and below were taken from the monograph by R T Sanderson *Chemical Bonds and Bond Energy* (New York: Academic Press, 1976).

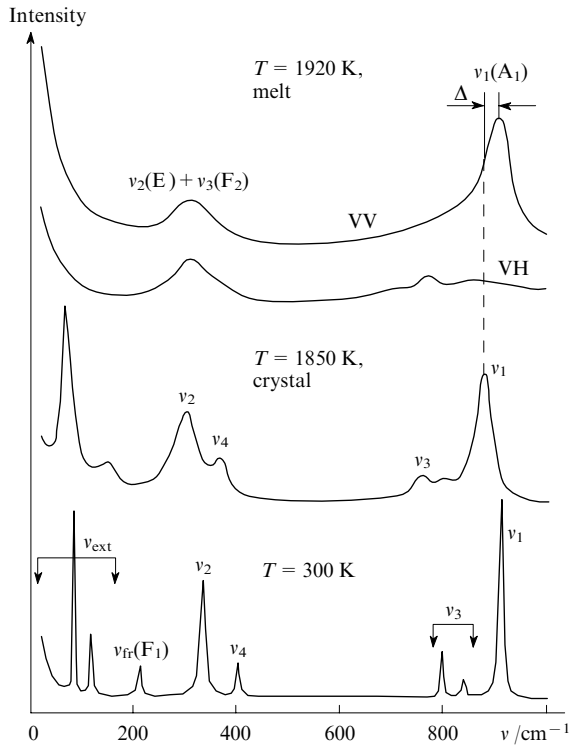


Figure 11. Temperature-dependent non-polarised Raman spectra of $CaWO_4$ crystals and polarised Raman spectra of $CaWO_4$ melt.[26]

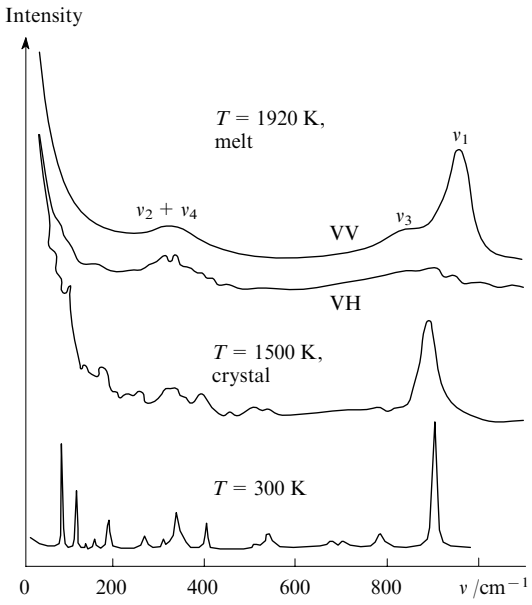


Figure 12. Temperature-dependent non-polarised Raman spectra of $ZnWO_4$ crystals and polarised Raman spectra of $ZnWO_4$ melt.[26]

nearly the same electronegativity as lead, whereas the atomic mass of lead is far larger than that of zinc and other cations under consideration. It is of note that the crystal structures of zinc molybdate and tungstate differ from that of scheelite. The molybdenum and tungsten atoms therein are octahedrally coordinated by the oxygen atoms.[33] However it was established that their coordination changes to the tetrahedral one upon melting (Fig. 12).

Therefore Raman studies of melts make it possible to separate the effects of the cation mass and electronegativity on the Raman frequencies. Frequencies of the $\nu_1(A_1)$, $\nu_2(E)$, $\nu_3(F_2)$ and $\nu_4(F_2)$ vibrational modes as a function of the cation electronegativity for melts of metal molybdates and tungstates are shown in Fig. 13. Frequencies of all these vibrational modes increase with an increase in the electronegativity in the Ba – Sr – Ca – Zn series thus indicating that it is the cation electronegativity that mainly determines the force constants corresponding to the internal vibrations within the $[MoO_4]$ and $[WO_4]$ groups. In contrast, the reduced mass of the M – O pair only weakly influences the vibrational frequencies within these groups for any M^{2+} except for Pb^{2+}. The vibrational frequencies of the $[MoO_4]$ and $[WO_4]$ groups in the melts of $PbMoO_4$ and $PbWO_4$ are drastically diminished with respect to compounds of other cations. Taking this into account, it might be suggested that the influence of a high electronegativity of Pb^{2+} on the Raman frequencies of the $[MoO_4]$ and $[WO_4]$ groups is effectively compenstated by a large reduced mass of the Pb – O pair.

The above results imply that the cation radius, mass and electronegativity jointly influence the internal vibrational frequencies of the tetrahedral groups not only in the crystalline but also in the molten state, where these quasi-molecular groups experience a spherically symmetric crystal field. This effect has not been considered so far (see, for instance, Ref. 30). Only the spectra of $PbMoO_4$ and $PbWO_4$ deviate from the common trend for both crystals and melts (see Figs 9, 10 and 13). This can be explained by the prevailing influence of a large mass of the lead atom on the vibrational frequencies of the $[MoO_4]$ and $[WO_4]$ groups. Meanwhile, no strong mass dependence is observed in the Ba – Sr – Ca series. A monotonic increase in the internal vibrational frequencies for the melts of Ba-, Sr- and Ca-derived scheelites is totally consistent with an increase in the electronegativity of these cations (see Fig. 13). It is of note that the highest-frequency totally symmetric mode, $\nu_1(A_g)$, demonstrates the reverse trend in the crystalline state (see Figs 9 and 10). This effect was referred [34] to as the 'negative mass dependence'. This dependence can be rationalised neither by an elongation of the Mo – O and W – O bonds due to a lattice dilatation nor by a decrease in the cation electronegativity. Both these factors would give rise to a decrease in the $\nu_1(A_g)$ frequency in the series of Ca – Sr – Ba scheelites, which is in direct contradiction to the experimental observations. Such a behaviour of the Raman frequencies can be explained assuming that it is the Davydov

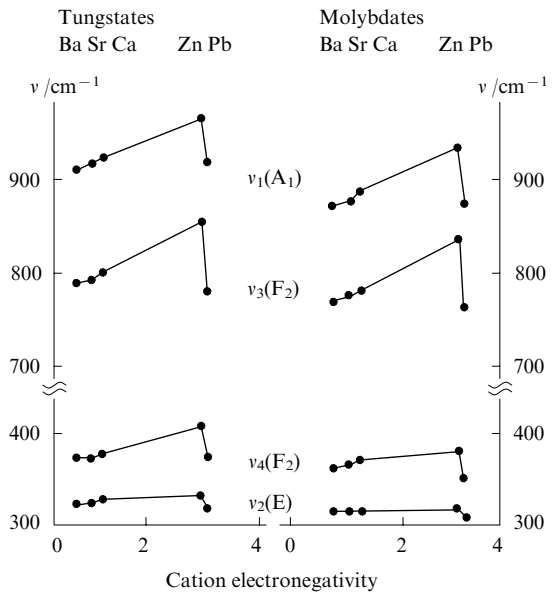


Figure 13. Changes in the Raman frequencies for melts of Ca, Sr, Ba, Zn and Pb molybdates and tungstates at 1920 K as a function of the cation electronegativity.[26]

splitting that dominantly affects the $\nu_1(A_g)$ frequency. For the scheelite structures, the Davydov splitting gives rise to a splitting of the $\nu_1(A_g)$ mode into two components, A_g and B_u [see the expression (2)]. Provided that the 'silent' component $\nu_1(B_u)$ corresponds to a higher energy than $\nu_1(A_g)$, the frequency corresponding to the lower-lying $\nu_1(A_g)$ mode should increase with a decrease in the splitting gap $\Delta E = \nu_1(B_u) - \nu_1(A_g)$. According to the results by Scott,[34] the splitting gap ΔE depends on the Mo – Mo and W – W interatomic distances in the crystal structures. An increase in these distances coupled with a lattice dilatation gives rise to a decrease in ΔE and, respectively, to an increase in the $\nu_1(A_g)$ frequency. The problem is that ΔE cannot be directly determined from experimental data, since the $\nu_1(B_u)$ is inactive in both Raman and IR absorption spectra. Basiev *et al.*[26] utilised high-temperature Raman spectroscopy to estimate ΔE. Indeed, in the case of melts, the spontaneous Raman scattering spectra are not affected by the Davydov splitting and the vibrational modes of the MoO_4 and WO_4 groups appear unsplit. A frequency shift of the $\nu_1(A_g)$ mode upon melting can directly be determined from the temperature dependence of Raman spectra

$$\Delta = \nu_1(A_g)_{cryst} - \nu_1(A_g)_{melt}\,.$$

Assuming that the Davydov splitting of ν_1 is symmetric, the splitting gap ΔE can be estimated as 2Δ. The experimental temperature dependences of the $\nu_1(A_g)$ frequencies over a wide temperature range from 77 K to above the melting points for a series of molybdates and tungstates are plotted in Fig. 14. It is apparent that the $\nu_1(A_g)$ frequency demonstrates a jump-like increase upon melting for the majority of scheelites, whereas it changes rather smoothly for $BaMoO_4$ and $BaWO_4$. This strongly suggests that the $\nu_1(A_g)$ frequency in the scheelite crystals is smaller than the $\nu_1(B_u)$ frequency. The magnitudes of the Davydov splitting estimated under the assumption that $\Delta E = 2\Delta$ are listed in Table 6 (calculated based on the experimental data from Fig. 14). The data allow one to trace the character of changes in ΔE along the series of scheelites (both molybdates and tunstates). The splitting increases with a decrease in the Mo – Mo and W – W interatomic distances in the unit cell. It turns to zero in the case of large unit cells of $BaMoO_4$ and $BaWO_4$ and reaches the maximum of 52 – 58 cm^{-1} for the smallest unit cells of $CaMoO_4$ and $CaWO_4$ (see Table 6). Therefore it is the Davydov splitting that is responsible for a decrease in the $\nu_1(A_g)$ frequency in the series of Ba – Sr – Ca scheelites. The influence of this splitting on the $\nu_1(A_g)$ frequency prevails over all other factors involved.

The influence of various crystal-chemical factors on the spectral widths ($\Delta\nu_R$) of Raman lines has also been analysed in detail.[26] The values of $\Delta\nu_R$ corresponding to the $\nu_1(A_g)$ vibrational modes as a function of temperature for a series of molybdates and tungstates in both the crystalline and molten states are plotted in Fig. 15. In the scheelite crystals, $\Delta\nu_R$ is virtually linearly dependent on the temperature. Meanwhile, the spectral line widths of all scheelites increase drastically upon melting. This trend in $\Delta\nu_R$ was attributed[26] to a homogeneous broadening of Raman lines due to the dephasing and depopulation of the $\nu_1(A_g)$ vibrational modes. A substantial difference in the line widths between molybdates and tungstates, on the one hand, and nitrates, on the other hand, can be rationalised based on the different energy diagrams of the internal vibrons for the MoO_4 or WO_4 tetrahedra and the NO_3 triangles, which gives rise to different degeneracies of the phonon relaxation processes. In particular, the energy gap between the $\nu_1(A_g)$ mode and adjacent modes in $Ba(NO_3)_2$ is ~ 300 cm^{-1}. In such a case, a three-phonon relaxation is impossible and thus four-phonon relaxation processes characterised by low probabilities prevail. As a consequence, the experimental Raman spectra reveal

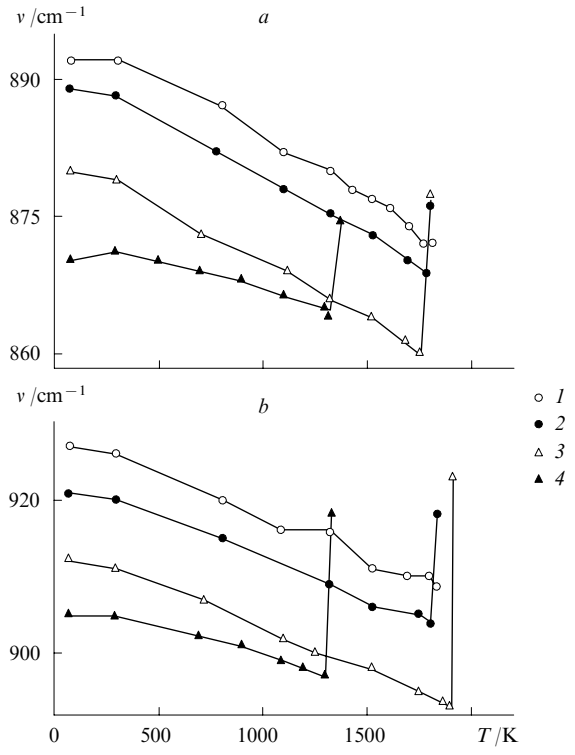


Figure 14. Changes in the Raman frequency of the $\nu_1(A_g)$ mode for homologous series of barium (*1*), strontium (*2*), calcium (*3*) and lead (*4*) molybdates (*a*) and tungstates (*b*) in the crystalline and molten states as a function of temperature.[26]

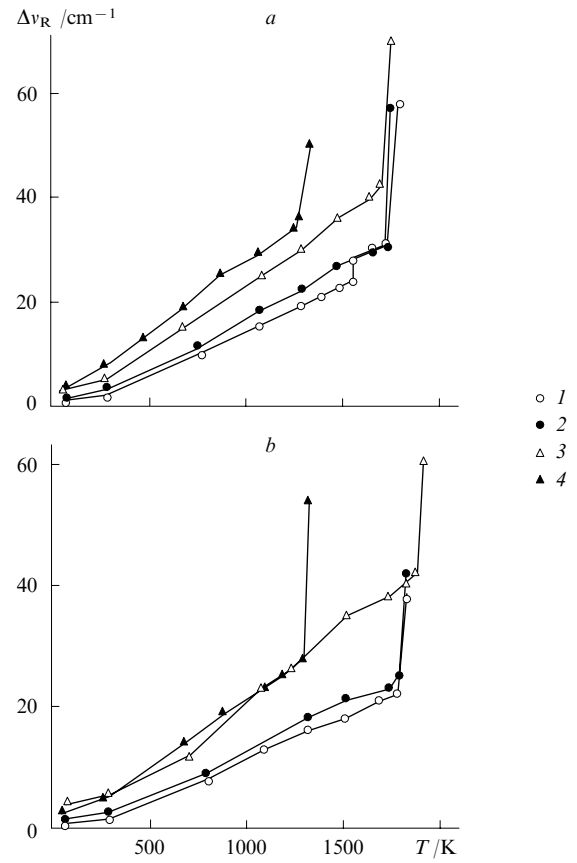


Figure 15. Changes in the widths of the Raman lines corresponding to the $\nu_1(A_g)$ mode for homologous series of barium (*1*), strontium (*2*), calcium (*3*) and lead (*4*) molybdates (*a*) and tungstates (*b*) as a function of temperature.[26]

a small homogeneous broadening and an extremely narrow line corrsponding to a large Σ_{peak} value. In the case of scheelites, the energy gap is 30 – 130 cm^{-1} and 70 – 150 cm^{-1} for molybdates and tungstates, respectively. At these energy gap values, the phonon relaxation is already dominated by three-phonon processes that are characterised by higher probabilities, which gives rise to a substantial homogeneous broadening of spectral lines corresponding to the internal vibrations.

A careful profile analysis of the $v_1(A_g)$ vibrational lines in the Raman spectra of a series of molybdates and tungstates measured under identical conditions revealed a continuous line narrowing in the Ca – Sr – Ba series (Fig. 16), which correlates with a decrease in the Davydov splitting and an increase in the cation mass. Lead molybdate and tungstate strongly deviate from the common trend showing an abnormal increase in $\Delta v_1(A_g)$, which can be explained by an increase in the Davydov splitting for the heavy but small lead cation as opposed to the heavy but large barium cation. Another prominent anomaly observed in the spectra of lead molybdate and tungstate by Basiev *et al.*[35] is related to their integral Raman scattering intensity. The experimental intensity of the $v_1(A_g)$ line was severalfold higher than that for other scheelites and the most intense scattering was observed in the orthogonal geometry, *i.e.*, with $\boldsymbol{E} \perp C4$ (Table 7).

Based on the results of temperature-dependent spontaneous Raman scattering measurements performed over a wide temperature range, the following conclusions can be derived:

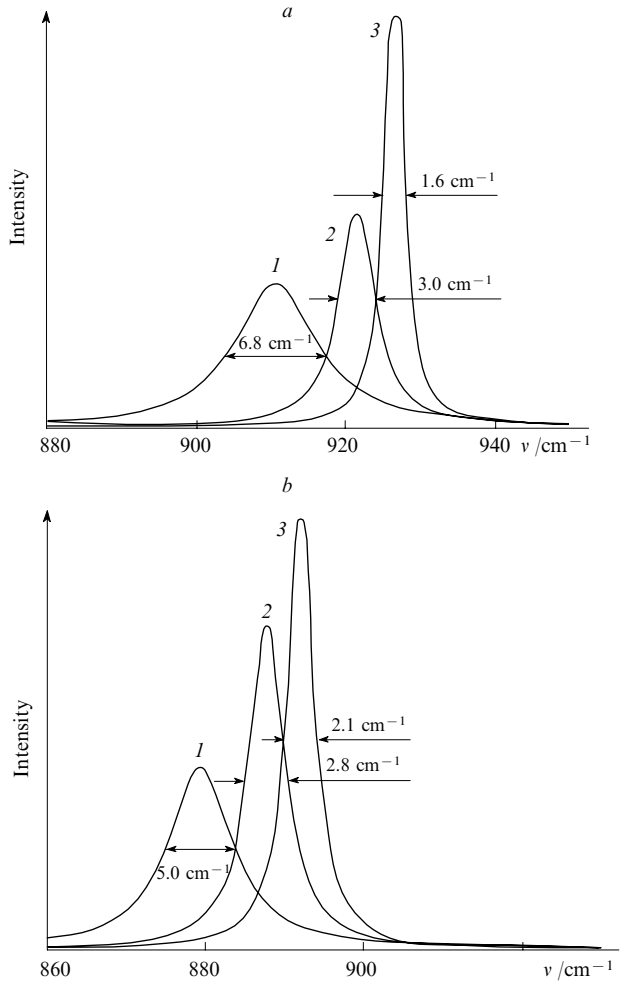


Figure 16. Room-temperature Raman line profiles [corresponding to the $v_1(A_g)$ mode] for calcium (*1*), strontium (*2*) and barium (*3*) tungstates (*a*) and molybdates (*b*).

— parameters of vibrational spectra of crystals with the scheelite structure are dependent on the mass, size and electronegativity of the cation M;

— the cation mass factor prevails in the case of low-energy external vibrational modes;

— the internal vibrational frequencies of the MoO_4 and WO_4 groups are primarily dependent on the unit cell parameters and the degree of covalency of the M – O bonds;

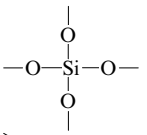
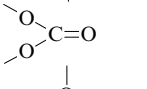
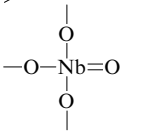
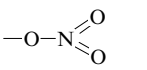
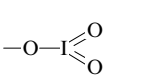
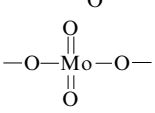
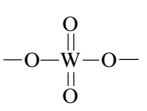
— the Davydov splitting of totally symmetric $v_1(A_g)$ vibrational modes in the tetrahedral MoO_4 and WO_4 groups continuously increases in the Ba – Sr – Pb – Ca series.

Table 7. Abnormally high Raman scattering cross-sections Σ_{peak} and Σ_{int} for $PbWO_4$ and $PbMoO_4$ crystals.

Crystal	Polarisation of the pumping radiation	Σ_{peak} (%)	Σ_{int} (%)
$BaWO_4$	$\boldsymbol{E} \parallel C4$	64	47
	$\boldsymbol{E} \perp C4$	52	38
$PbWO_4$	$\boldsymbol{E} \parallel C4$	65	120
	$\boldsymbol{E} \perp C4$	97	171
$PbMoO_4$	$\boldsymbol{E} \parallel C4$	64	203
	$\boldsymbol{E} \perp C4$	146	397

The widths of Raman lines depend on specific features of the crystal lattice and the nature of an M^{2+} cation. A combination of 'lightweight' cations with short interionic distances gives rise to a substantial line broadening. The narrowest lines corresponding to the $v_1(A_g)$ modes are observed for the case of heavy cations with large ionic radii, *i.e.*, in $BaMoO_4$ and $BaWO_4$ (2.1 cm^{-1} and 1.6 cm^{-1}, respectively), which results in the record high SRS gain coefficients. The abnormal trends in the changes of vibrational modes for $PbWO_4$ and $PbMoO_4$ cannot be explained taking into account only atomic masses, ionic radii and structure type. A more careful in-depth analysis of effects related to the character of

Table 8. Integral Raman scattering cross-sections (relative to diamond) in crystals of different compounds and effective radii of the oxygen-containing anions.

Group of compounds	Σ_{int} (%)	Anion	Effective radius /Å
Silicates (SiO_2)	2.2		2.3
Carbonates ($CaCO_3$)	6		1.8
Niobates ($LaNbO_4$)	22		2.5
Nitrates [$Ba(NO_3)_2$]	21		1.9
Iodates ($LiIO_3$)	54		2.5
Molybdates ($MMoO_4$)	52 – 64		2.5
Tungstates (MWO_4)	47 – 52		2.6

the Pb–O chemical bonds is required. The integral line intensity represents the most difficult problem as regards the interpretation and prediction of Raman scattering and SRS parameters. This problem is additionally complicated by the fact that an incident radiation generates simultaneously several Raman components characterised by different intensities in the vast majority of crystalline media, which effectively gives rise to a distribution of the converted radiation energy over several vibrational modes (in contrast to, for instance, diamond, where all scattered energy is concentrated in a single line profile).

The integral intensities Σ_{int} corresponding to internal vibrational lines of quasi-molecular ions in different types of crystals are compiled in Table 8 together with their respective effective radii.[36] A correlation between Σ_{int} and the effective anion radius exists: Σ_{int} increases with an increase in the anion size. In particular, Σ_{int} in crystals of molybdates, tungstates, niobates and iodates significantly exceeds those in such compounds as borates, carbonates and nitrates.

V. SRS converters and lasers based on novel crystals

According to the data considered in previous sections, it can be concluded that an efficient SRS conversion of the laser radiation (that is the conversion with a high efficiency) can be realised in materials complying with the following requirements:

— large peak and integral Raman scattering cross-sections;

— low optical losses of both pumping radiation and SRS radiation; this implies that the crystals have to be optically homogeneous and defect-free and have a wide spectral window of transparency;

— crystals should be mechanically strong and chemically stable; in particular, they should provide a high radiation damage threshold and do not degrade in terms of optical homogeneity under atmospheric humidity, sun light, *etc*.

Below we give a few examples of successful application of novel crystals in SRS lasers.

1. Nanosecond SRS lasers with $BaWO_4$ and $SrWO_4$ crystals

Zverev *et al*.[37] reported on the results of comparative tests of novel $BaWO_4$ crystals and well-known $Ba(NO_3)_2$ and $KGd(WO_4)_2$ crystals. The crystal elements made from $BaWO_4$, $Ba(NO_3)_2$ and $KGd(WO_4)_2$ were placed into a Fabry–Perot resonator with a length of 9 cm. The input mirror had a reflection coefficient of 5% and 98% at the pumping radiation wavelength of 1.064 μm and in the range of the generated Stokes components, *i.e*., $\lambda = 1.1-1.25$ μm, respectively. The output mirror had a reflection coefficient $R_{1.0-1.2} = 55\%$. As a pumping source, a single-mode Nd-doped yttrium–aluminium garnet laser ($YAG:Nd^{3+}$) with a passive $LiF:F_2^-$ Q-switch was used. The pulse duration was 20 ns at a repetition rate of 10 s^{-1}. The efficiency of SRS radiation was 26% and 20.5% with $Ba(NO_3)_2$ and $BaWO_4$ crystals, respectively. In both cases, the slope efficiency exceeded 75% at nearly identical SRS thresholds. It is of note that the SRS properties of $BaWO_4$ are polarised; in particular, the efficiency was higher for $\boldsymbol{E} \| C4$ and lower for $\boldsymbol{E} \perp C4$. The $KGd(WO_4)_2$ crystals demonstrated a higher SRS threshold and a slope efficiency of only 45% under strictly identical experimental conditions.

The SRS-based frequency conversion of radiation produced by an Nd-doped gadolinium–gallium garnet laser was also elucidated.[38] A $BaWO_4$-based SRS converter shifted the incident laser wavelength from 1.0621 μm to 1.1779 μm. As a result of the conversion with a slope efficiency above 30%, pulses with an energy of 15 mJ at a power in the MW range and a repetition rate of 10 s^{-1} were produced.

The efficiency of an $SrWO_4$-based SRS laser was characterised under similar conditions.[39] Strontium tungstate crystals can be doped with a large amount of neodymium. In such a case, the same crystal can simultaneously serve for the generation of the laser radiation with $\lambda = 1.06$ μm on Nd^{3+} sites and its SRS conversion to $\lambda = 1.18$ μm. This functional integration admits a significant decrease in the size of the laser device and strongly enhances the reliability of its operation.

2. Nanosecond SRS lasers in the mid-IR region with $BaWO_4$ crystals

$BaWO_4$ crystals are highly transparent in the intermediate IR spectral range, which can be exploited in the design of lasers generating radiation with a wavelength within 2–5 μm. As has been mentioned above, this spectral range is extremely important for practical applications but remains poorly developed. The major problem there is that the longest possible wavelengths of pumping radiation have to be used in a combination with the second (or even the third) Stokes components of the Raman spectrum, since a typical SRS fruquency shift is on the order of ~ 1000 cm^{-1}. Furthermore, the SRS gain coefficient rapidly decreases with an increase in the pumping wavelength. Basiev *et al*.[40] utilised crystal elements made from $BaWO_4$ with a length of 42 mm to convert the pumping radiation of 1.34 μm generated by a $YAG:Nd^{3+}$ laser equipped with an acoustooptic Q-switch. The SRS-converted spectrum is shown in Fig. 17. The spectrum reveals the first (1.53 μm), second (1.78 μm) and third (2.13 μm) Stokes components. The slope efficiency for the conversion of the pumping energy (1.34 μm) into the first and the second Stokes components was higher than 22%.

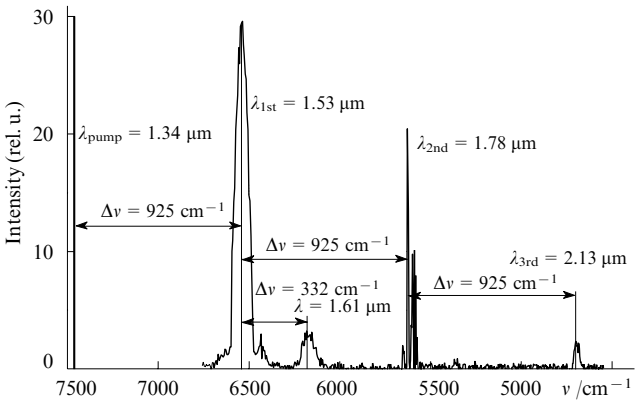


Figure 17. The SRS generation spectra of $BaWO_4$ crystals pumped by a neodymium-doped yttrium–aluminium garnet laser operated at a wavelength of 1.34 μm.[40]

Recently, a significant advancement towards the mid-IR region has been achieved.[41] It relates to the SRS spectral conversion of nanosecond laser pulses at wavelengths of 1.56 μm and 1.91 μm with $BaWO_4$ crystals. It has been shown that the pumping radiation with $\lambda = 1.56$ μm undergoes a multi-stage conversion into the first, second, third and fourth Stokes SRS components corresponding to wavelengths of 1.82, 2.19, 2.75 and 3.69 μm, respectively. The generated SRS components are shown in Fig. 18 in a comparison with the transmission spectrum of $BaWO_4$ crystals.

In the case of nanosecond pumping pulses with $\lambda = 1.91$ μm, the first Stokes SRS component with 2.32 μm was successfully generated. It is important that the $BaWO_4$ crystal utilised in the converter was only 27 mm long.

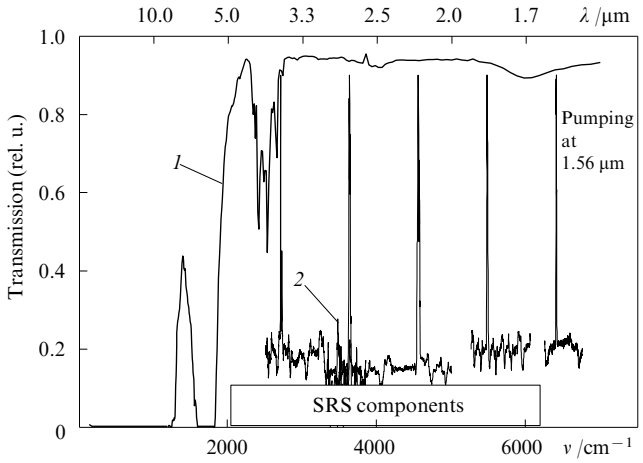


Figure 18. A transmission spectrum of $BaWO_4$ crystals (*1*) and the $BaWO_4$ Raman laser oscillation spectra in the mid-IR region (*2*).

3. The SRS conversion of picosecond laser pulses with $BaWO_4$ crystals

Černy *et al.*[42] accomplished a comparative analysis of the performace of $BaWO_4$, $KGd(WO_4)_2$ and $KY(WO_4)_2$ crystals in the SRS conversion of picosecond pulses. The pumping radiation was characterised by wavelengths of 0.53 μm and 1.064 μm and pulse durations of 28 and 40 ns, respectively. In the case of the green pumping ligth (0.53 μm), the gain coefficients were 14.4 cm $(GW)^{-1}$, 11.5 cm $(GW)^{-1}$ and 18.7 cm $(GW)^{-1}$ with $BaWO_4$, $KGd(WO_4)_2$ and $KY(WO_4)_2$ crystals, respectively. While the gain coefficient provided by the $BaWO_4$ crystal was three times larger than that with $KGd(WO_4)_2$ in the steady-state SRS mode, its advantage was not as evident in the picosecond mode. This is explained by the narrower Raman line and shorter relaxation time in $BaWO_4$ as compared with the respective values in $KGd(WO_4)_2$. A different situation is observed when the $BaWO_4$ performance is compared with that of $Ba(NO_3)_2$. For nanosecond pumping pulses (in the steady-state mode), the gain coefficient provided by the $BaWO_4$ crystal was 20% – 30% lower than that with $Ba(NO_3)_2$. Meanwhile, in the picosecond (transient) mode, $BaWO_4$ performs three times better than $Ba(NO_3)_2$. The gain coefficients for picosecond pumping pulses with $\lambda = 1.064$ μm were 3.8 cm $(GW)^{-1}$, 4.7 cm $(GW)^{-1}$ and 3 cm $(GW)^{-1}$ for $BaWO_4$, $KY(WO_4)_2$ and $KGd(WO_4)_2$, respectively. The maximum efficiency of a working element made from $BaWO_4$ with a length of 30 mm for picosecond pumping pulses with $\lambda = 0.53$ μm was 30% for the first Stokes component. The respective value for a $KGd(WO_4)_2$ crystal with a length of 40 mm was only 18%. According to the detailed measurements on the efficiency of the SRS generation,[43] the efficiency of the conversion of pulsed pumping radiation with a wavelength of 1.064 μm and a pulse duration of 50 ps into the first Stokes component of 1.180 μm increases from 25% to 35% on going from a one-pass to a two-pass optical scheme. When the $BaWO_4$ element was placed into a resonator with a length of 38 cm equipped with an output mirror with the optimised transmission spectrum, the absolute efficiency increased to 55%, whereas the slope efficiency (estimated by the slope) reached nearly 100%.[44]

4. SRS frequency converters and lasers with $PbWO_4$, $PbMoO_4$ and $PbMoO_4:Nd^{3+}$ crystals

Kaminskii *et al.*[45,46] studied radiation of an SRS laser with $PbWO_4$ crystals pumped by a $YAG:Nd^{3+}$ pulsed laser with $\lambda = 1.064$ μm and a pulse duration of 100 ps. The conversion efficiency of 20% was achieved at an energy of the pumping pulses of 5 mJ using a resonator with planar-convex mirrors having a length of 200 mm. The length of a working $PbWO_4$ element was 30 mm. The same authors reported on the SRS conversion of pulsed green radiation with a wavelength of 0.53 μm and a pulse duration of 30 ps. The $PbWO_4$ crystal provided a gain coefficient of 8.4 cm $(GW)^{-1}$.

Another study[47] was devoted to the generation of SRS by one or two elements made from $PbWO_4$ with a length of 45 mm placed into a ring resonator. The pumping was achieved with the first harmonic of a pulsed $YAG:Nd^{3+}$ laser with a pulse duration of 7 ns. With one element in the resonator, the energy of SRS radiation was 5.3 mJ at an energy of pumping pulses of 36 mJ (which is already close to the laser damage threshold of $PbWO_4$ crystals). The conversion efficiency of 20% was achieved with two elements in the resonator.

Atypically high values of Σ_{peak} and Σ_{int} observed for $PbMoO_4$ crystals make it a promising candidate for achieving unprecedentally high efficiencies of the SRS conversion for both nanosecond and picosecond pulse duration regimes. Furthermore, the $PbMoO_4$ crystal lattice easily accomodates a large amount of doping rare-earth elements, which makes it possible to combine the laser light generation and its SRS conversion within one crystal. According to a series of recent publications,[27,35,48] these predictions are well justified. The following experiments have been reported:

— the generation of SRS in $PbMoO_4$ crystals as a function of the sample orientation relative to the polarisation vector of the incident radiation;

— the laser light generation by the Nd^{3+} ions in $PbMoO_4:Nd^{3+}$ in the free-running mode;

— the laser light generation by the Nd^{3+} ions in the Q-switched mode;

— the laser light generation by the Nd^{3+} ions with its simultaneous conversion to the first Stokes SRS component.

The pumping was achieved with a semiconductor laser diode emitting at a wavelength of 0.808 μm and a power of 1.5 W. The radiation of the laser diode was fully linearly polarised and pulsed with a pulse duration of 250 μs at a repetition rate of 5 s^{-1}). As laser elements, $PbMoO_4:Nd^{3+}$ crystals with neodymium concentrations of 0.3 mass % and 2 mass % were employed. Rectangular plates with thicknesses of 1 mm were cut perpendicular to the crystallogaphic *a* axis. In the free-running oscillation mode, the radiation with a wavelength of 1.0556 μm was produced. The differential generation efficiency was 53% for the sample with 0.3 mass % of Nd. In the case of the sample with 2 mass % of Nd, an average oscillation power of 0.65 W was achieved.

Q-Switching was accomplished with a passive shutter based on lithium fluoride crystals with F_2^- colour centres. Under these conditions, a pulsed SRS oscillation mode was realised with a pulse repetition rate of $(7.5-190)\times10^3$ s^{-1} at a peak power of ~2 kW and an average power of ~0.36 W. The pulse duration was from 8.7 ns to 1.4 ns. These results prove that $PbMoO_4:Nd^{3+}$ provides a high average power in the Q-switched operation mode (only 1.8 times lower than in the free-running oscillation mode).

In experiments on the self-conversion of the laser radiation generated by the neodymium ions in $PbMoO_4:Nd^{3+}$ into the SRS, the thickness of working elements was 3 mm. With a $LiF:F_2^-$ Q-switch, the first Stokes SRS component was observed at a wavelength of 1.163 μm. The output pulse energy was 6 μJ at a pulse duration of < 500 ps. This implies that the peak pulse power achived was higher than 12 kW.

Potential application fields of the novel SRS crystals and lasers on their base are comprehensively considered elsewhere.[49,50]

* * *

The recent experimental data on the SRS-based laser wavelength conversion considered above proves the significant predictive power of the approach to the search for novel SRS-active media described in the present review. The theoretical conclusions on the

frequencies and widths of SRS lines with their relation to the conversion efficiency of laser pulses with different durations are fully supported by experimental results.

The conclusions regarding the homologous series of alkali-earth metal molybdates and tungstates can be extended (with minor correction) to other homologous classes of inorganic compounds.

Therefore, the use of stimulated Raman scattering in crystals of inorganic compounds has a huge potential in solving the problem of the design of spectrally positioned laser sources.

The authors are grateful to L N Ershova and M N Basieva for help in the manuscript preparation.

References

1. T T Basiev, E V Zharikov, V V Osiko *Crystallogr. Rep.* **47** (Suppl. 1) 15 (2002)
2. C V Raman, K S Krishnan *Nature (London)* **121** 501 (1928)
3. G S Landsberg, L I Mandelshtam *Zh. Russ. Fiz.-Khim. O-va* **60** 335 (1928)
4. E J Woodbury, W K Ng *Proc. IRE* **50** 2367 (1962)
5. R W Hellwarth *Phys. Rev.* **130** 1850 (1963)
6. G Plachek *Releevskoe Rasseyanie i Raman-effekt* (Rayleigh Scattering and Raman Effect) (Khar'kov: GNTI Ukraina, 1935)
7. P G Zverev, T T Basiev, I V Ermakov, A M Prokhorov, in *Laser Methods of Surface Treatment and Modification: ALT'94. International Conference* Vol. 2498 (Eds A M Prokhorov, V I Pustovoy) (Washington, DC: SPIE, 1994) p. 164
8. Y Wang *Phys. Rev.* **182** 482 (1969)
9. G Eckhardt, D P Bortfeld, M Geller *Appl. Phys. Lett.* **3** 137 (1963)
10. A S Eremenko, S N Karpukhin, A I Stepanov *Kvantovaya Elektron.* **7** 196 (1980) [*Quantum Electron.* **10** 113 (1980)]
11. S N Karpukhin, A I Stepanov *Kvantovaya Elektron.* **13** 1572 (1986)] [*Quantum Electron.* **16** 1027 (1986)]
12. T T Basiev, V N Voitsekhovskii, P G Zverev, F V Karpushko, A V Lyubimov, S B Mirov, V P Morozov, I V Mochalov, A A Pavlyuk, G V Sinitsyn, V E Yakobson *Kvantovaya Elektron.* **14** 2452 (1987)] [*Quantum Electron.* **17** 1560 (1987)]
13. P G Zverev, T T Basiev, in *Trudy Mezhdunarodnoi Konferentsii 'Optika Lazerov', Sankt-Peterburg, 1993* (Proceedings of International Conference 'Laser Optics', St Petersburg, 1993) Vol. 2, p. 363
14. P G Zverev, J T Murray, R C Powell, R J Reeves, T T Basiev *Opt. Commun.* **97** 59 (1993)
15. K Andryunas, Yu K Vishchakas, V Kabelka, I V Mochalov, A A Pavlyuk, G T Petrovskii, V P Sirus *Pis'ma Zh. Eksp. Teor. Fiz.* **42** 410 (1985) [a]
16. T T Basiev, A A Sobol, P G Zverev, V V Osiko, R C Powell *Appl. Opt.* **38** 594 (1999)
17. T T Basiev *Usp. Fiz. Nauk* **169** 1149 (1999) [*Physics-Uspekhi* **42** 1051 (1999)]
18. Yu K Vishchakas, I V Mochalov, A V Mikhailov, R F Klevtsova, A V Lyubimov *Lietuvos Fiz. Rinkinys* **28** 224 (1988)
19. P G Zverev, W Jia, H Liu, T T Basiev *Opt. Lett.* **20** 2378 (1995)
20. P G Zverev, T T Basiev *Kvantovaya Elektron.* **22** 1241 (1995) [*Quantum Electron.* **25** 1204 (1995)]
21. J Czochralski *Z. Phys. Chem.* **92** 219 (1918)
22. L I Ivleva, N V Bogodaev, N M Polozkov, V V Osiko *Opt. Mater.* **4** 168 (1995)
23. I S Voronina, L I Ivleva, V V Osiko, N M Polozkov, in *Proceeding of SPIE Solid State. Crystals 2002. Crystalline Materials for Optoelectronics, London, 2003* Vol. 5136, p. 10
24. L I Ivleva, T T Basiev, I S Voronina, P G Zverev, V V Osiko, N M Polozkov *Opt. Mater.* **23** 439 (2003)
25. I S Voronina, L I Ivleva, T T Basiev, P G Zverev, N M Polozkov *J. Optoelectron. Adv. Mater.* **5** 882 (2003)
26. T T Basiev, A A Sobol, Yu K Voron'ko, P G Zverev *Opt. Mater.* **15** 205 (2000)
27. M B Kosmyna, B P Nazarenko, V M Puzikov, V V Osiko, T T Basiev, S V Vasil'ev, M E Doroshenko, in *International Conference 'Crystal Materials 2005' (ICCM 2005) (Abstracts Book), Kharkov, 2005* p. 181
28. Yu K Voron'ko, A B Kudryavtsev, V V Osiko, A A Sobol', in *Rost Kristallov* (Crystal Growth) (Eds Kh S Bagdasarov, E L Lube) (Moscow: Nauka, 1988) Vol. 16, p. 178
29. S P S Porto, J F Scott *Phys. Rev.* **157** 716 (1967)
30. J F Scott *J. Chem. Phys.* **48** 874 (1968)
31. H Kanamory, S Hayashi, Y Ykeda *J. Phys. Soc. Jpn.* **36** 511 (1964)
32. A N Lazarev, A P Mirgorodskii, I S Ignat'ev *Kolebatel'nye Spektry Slozhnykh Oksidov* (Vibration Spectra of Complex Oxides) (Leningrad: Nauka, 1975)
33. O S Filippenko, E A Pobedimskaya, N N Belov *Kristallografiya* **13** 163 (1968) [b]
34. J F Scott *J. Chem. Phys.* **49** 98 (1968)
35. T T Basiev, P G Zverev, A Ya Karasik, V V Osiko, A A Sobol', D S Chunaev *Zh. Eksp. Teor. Fiz.* **126** 1073 (2004) [c]
36. T T Basiev *Fiz. Tv. Tela* **47** 1354 (2005) [d]
37. P G Zverev, T T Basiev, A A Sobol', V V Skornyakov, L I Ivleva, N M Polozkov, V V Osiko *Kvantovaya Elektron.* **30** 55 (2000) [*Quantum Electron.* **30** 55 (2000)]
38. P G Zverev, T T Basiev, M E Doroshenko, V V Osiko, in *OSA Trends in Optics and Photonics Series* Vol. 34 (Washington, DC: Optical Society of America, 2000) p. 348
39. T T Basiev, P G Zverev, A A Sobol, V V Osiko, in *Technical Digest of Advanced Solid State Lasers* (Washington, DC: Optical Society of America, 2002) MB10
40. T T Basiev, M E Doroshenko, V V Osiko, S E Sverchkov, B I Galagan *Laser Phys. Lett.* **2** (5) 237 (2005)
41. T T Basiev, M N Basieva, M E Doroshenko, V V Fedorov, V V Osiko, S V Mirov *Laser Phys. Lett.* **3** 17 (2006)
42. P Černy, P G Zverev, H Jelinkova, T T Basiev *Opt. Commun.* **177** 397 (2000)
43. P Černy, H Jelinkova, M Miyagi, T T Basiev, P G Zverev, in *Solid State Lasers XI. Proceedings of SPIE* Vol. 4630 (Washington, DC: SPIE, 2002) p. 108
44. P Černy, H Jelinkova, J Sulc, P G Zverev, T T Basiev *Prog. Quantum Electron.* **28** 113 (2004)
45. A A Kaminskii, H J Eichler, K Ueda, N V Klassen, B S Redkin, L E Li, J Findeisen, D Jaque, J Garcia-Sole, J Fernandez, R Balda *Appl. Opt.* **38** 4533 (1999)
46. J Findeisen, H J Eichler, A A Kaminskii *IEEE J. Quantum Electron.* **35** 173 (1999)
47. A A Kaminskii, C L McCray, H R Lee, S W Lee, D A Temple, T H Chyba, W D Marsh, J C Barnes, A N Annanenkov, V D Legun, H J Eichler, G M A Gad, K Ueda *Opt. Commun.* **183** 277 (2000)
48. T T Basiev, S V Vassiliev, M E Doroshenko, V V Osiko, V M Puzikov, M B Kosmyna *Opt. Lett.* **31** 65 (2006)
49. T T Basiev, V V Osiko, A M Prokhorov, E M Dianov *Top. Appl. Phys.* **89** 35 (2003)
50. T T Basiev, R C Powell, in *Handbook of Laser Technology and Applications* (Eds C E Webb, J D C Jones) (London: Institute of Physics Publishing, 2004) Vol. 2, Ch. B-1.7, P. 469

[a] — *J. Exp. Theor. Phys. Lett. (Engl. Transl.)*
[b] — *Crystallogr. Rep. (Engl. Transl.)*
[c] — *J. Exp. Theor. Phys. (Engl. Transl.)*
[d] — *Phys. Solid State (Engl. Transl.)*